nature portfolio

https://doi.org/10.1038/s41561-021-00721-4

Supplementary information

Spatiotemporal clustering of great earthquakes on a transform fault controlled by geometry

In the format provided by the authors and unedited

Supplementary Information

The following covers the data used to derive the results for the paper 'Spatiotemporal clustering of great earthquakes on a transform fault controlled by geometry' by Jamie D. Howarth, Nicolas C. Barth, Sean J. Fitzsimons, Keith Richards-Dinger, Ursula Cochran, Glenn P. Biasi, Kate Clark, Robert Langridge, Kelvin Berryman, and Rupert Sutherland.

TABLE OF CONTENTS

SUPPLEMENTARY TEXT:

SUPPLEMENTARY FIGURES:

SUPPLEMENTARY TABLES:

Supplementary Discussion 1: sedimentology of Westland Lakes

The sedimentary archives of lakes in Westland, New Zealand are characterized by four lithofacies: layered silts, type 1 rapidly deposited layer (RDL), type 2 RDL and type 3 RDL (Supplementary Table 1 and Supplementary Fig. 1). These lithofacies are described in detail and interpreted with respect to depositional processes by Howarth et al.[1,2] and are summarized in Supplementary Table 1.

The sedimentary signature of the 1717 CE Alpine Fault earthquake in lakes Kaniere, Mapourika, Paringa and Ellery is characterized by an event sequence of a debrite (Type 1 RDL, absent in some instances), overlain by a turbidite (Type 2 RDL), which in turn is overlain by interbedded L2 and/or hyperpycnite (Type 3 RDL) deposits (Supplementary Figs. 2 and 3). This earthquake event sequence (EES) is indicative of subaqueous mass-wasting in the lake basin followed immediately by increased terrigenous sediment flux from the lake catchment. The period of increased sediment flux is inferred to be driven by landsliding on hillslopes that had to precede the deposition of this material in the lake[1-3]. Consequently, the subaqueous mass-wasting and increased terrigenous sediment flux recorded by event sequences are consistent with near synchronous disturbance of both hillslopes and subaqueous slopes[1-3]. The sedimentary response and inferred causative processes is precisely the landscape response that would be expected as a consequence high intensity shaking of the lakes and their catchments. Seismic shaking causes co-seismic landsliding within lake basins[4,5] and on hillslopes that results in years to decades of increased terrigenous sediment flux from catchments[3,6-8].

The facies composition of phases of postseismic increased terrigenous sediment flux varies between basins depending on the size of the influent fluvial tributaries. Increased terrigenous sediment flux is recorded as decimetre thick stacks of hyperpycnites overlying mass-wasting derived turbidites in basins such as the Windbag in Lake Paringa that have streams draining relatively large influent fluvial catchments (Supplementary Fig. 2). Conversely, in basins that lack major influent streams, such as the Hall Basin in Lake Paringa, the hyperpycnites are absent and the signature of increased terrigenous sediment flux is recorded by an increased abundance of L2 sediments.

The lack of thick stacks of hyperpycnites in basins that have no significant fluvial inflow provides an advantage for paleoseisemic reconstructions because it allows longer event records to be generated with the available Mackereth coring technology that is limited to the upper ~ 6 m of sedimentary fill. Here we present two new records, one from the Hall Basin of Lake Paringa (Supplementary Fig. 4) and the other from Lake Kaniere (Supplementary Fig. 5). These records complement existing archives from lakes Ellery[1] and Mapourika[2] providing a record that spans the entire 250 km length of the Alpine Fault's Central section. The facies architecture of Lake Paringa's Hall Basin and Lake Kaniere sedimentary records are composed of layered silts punctuated by EES. Earthquake event sequences in both records correlate to the last rupture of the Alpine Fault in 1717 CE (Supplementary Fig. 2 and 3). Trends in continuous grainsize, C:N ratios, dry bulk density, Ti concentration and CT number (a proxy of density) curves through the 1717 CE EES support the interpretation of co-seismic subaqueous mass-wasting followed by postseismic increases in the flux of clastic sediment to the lake (Supplementary Fig. 2). The essential features of EES are captured in the CT tomography and related CT units. Hence the CT data and imagery were used to identify EES through the sedimentary record (Supplementary Fig. 6 and 7). There are 12 EES in Lake Kaniere and 15 in Lake Paringa's Hall Basin, all of which have been dated precisely to facilitate inter-lake correlation with the nine EES recorded in Lake Ellery and seven in Lake Mapourika.

There are two complexities to the simple progression of EES separated by layered silts in the cores. The first is isolated turbidites (Type 2 RDL) that occur within the layered silts that separate EES. These turbidites are rare and much thinner than those within EES, although their structure is consistent with formation by subaqueous mass-wasting. The second complexity is multiple EES stacked in close succession or immediately over or under-lain by subaqueous mass-wasting derived turbidites (Type 2 RDL) (Supplementary Fig. 4). These stacked EES can be distinguished from the complexly bedded turbidites by the presence of discrete unit T3 caps that form as the finest fraction of sediment mobilised by the flow gradually settles out of the water column over the days to weeks[9]. In some instances, thin units of layered silts separate EES indicating years to decades elapsed between the triggering events. These EES stacks are most common in the sedimentary records of Lake Kaniere and to a lesser extent Lake Ellery, which are located at the southern and northern extents of the Alpine Fault's Central section respectively. Conversely, the records from lakes Paringa and Mapourika contain simple EES separated by thick layered silt units indicative of centuries of deposition. The stacked EES in lakes Kaniere and Ellery are most likely due to an increase in the frequency of earthquake-induced shaking at section boundaries due to moderate earthquakes that nucleate there or sequential earthquakes on adjacent Alpine Fault sections and/or adjoining faults.

Supplementary Table 1: Description and interpretation of facies found in cores from lakes Kaniere, Mapourika, Paringa and Ellery.

Lithofacies	Unit	Description	Classification*	Interpretation
Layered silt	L_2	20-1000 mm thick beds characterized by two units. L_1: 2-50 mm units of coarse to medium silt that has relatively high autochthonous organic content. L_2: 2-50 mm units of planar bedded, coarse to medium silt that have low organic content derived from terrigenous sources.	N/A	Formed by gradual accumulation of pelagic (L_1) and terrestrial (L_2) sediment.
	L_1			
Type 1 RDL	D_m	20-1000 mm thick beds of fine sandy gravels and/or deformed lacustrine sediments. Invariably overlain by type 2 RDL.	D_{m-2}	Debrite formed by deposition of subaqueous debris flow sediments.
Type 2 RDL	T_1	Up to 400 mm thick beds characterized by three distinct units. T_1: up to 100 mm thick basal unit of massive or planar bedded, medium sand to very coarse silt. T_2: 20-300 mm thick intermediate unit of massive, weakly normally or ungraded, coarse silt that thickens towards the basin centre. T_3: up to 100 mm thick, massive medium silt cap.	T_A to T_{B-2}	Turbidite formed by deposition from high density turbidity currents and associated turbulent suspension clouds formed by basin wide failure of lake deltas and slope sediments.
	T_2		T_{E-2} and/or T_{E-3}	
	T_3		N/A	
Type 3 RDL		Very fine sandy silt that normally grades into medium silt both of which contain terrigenous organic material. Always found interbedded with L_2 beds.	T_{E-2}	Hyperpycnites formed by hyperpycnal flows generated by discharge of sediment laden fluvial effluent.

*Sediment density flow classification from Talling et al. (ref.[10])

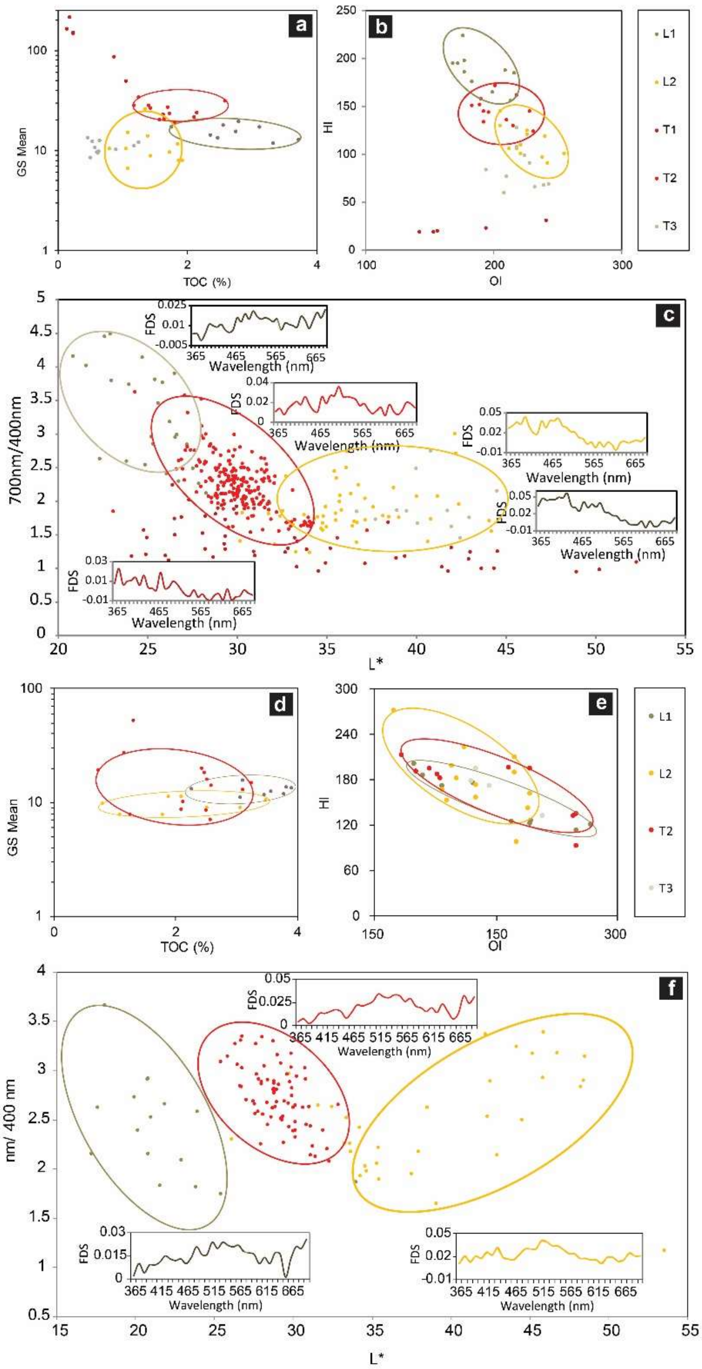

Supplementary Figure 1: Summary of Rock Eval pyrolysis, spectrophotometry and first derivative spectra (FDS) analyses on sedimentary facies from lakes Paringa (**a,b,c**) and Kaniere (**d, e, f**). **a, d:** Bivariate plot of mean grainsize against total organic carbon (TOC). **b, e:** Bivariate plot showing HI against OI. **c, f:** 700 nm/400 nm ratio (a proxy for organic matter content) against L* (luminosity), or the Q7/4 diagram. All bivariate plots show speciation of the sedimentary facies. Insets in C show FDS for each facies. The coloured ovals demonstrate the important distinction between L1 (brown) and L2 units (yellow) within the layered silt facies and that T2 units from type 2 RDL (red) plot between them, supporting the interpretation that type 2 RDL contain reworked lacustrine sediments. L1 unit sediments have FDS and HI:OI ratios characteristic of autochthonous organic material, unit L2 of clay rich terrigenous material and T2 intermediary between these two end members[11,12].

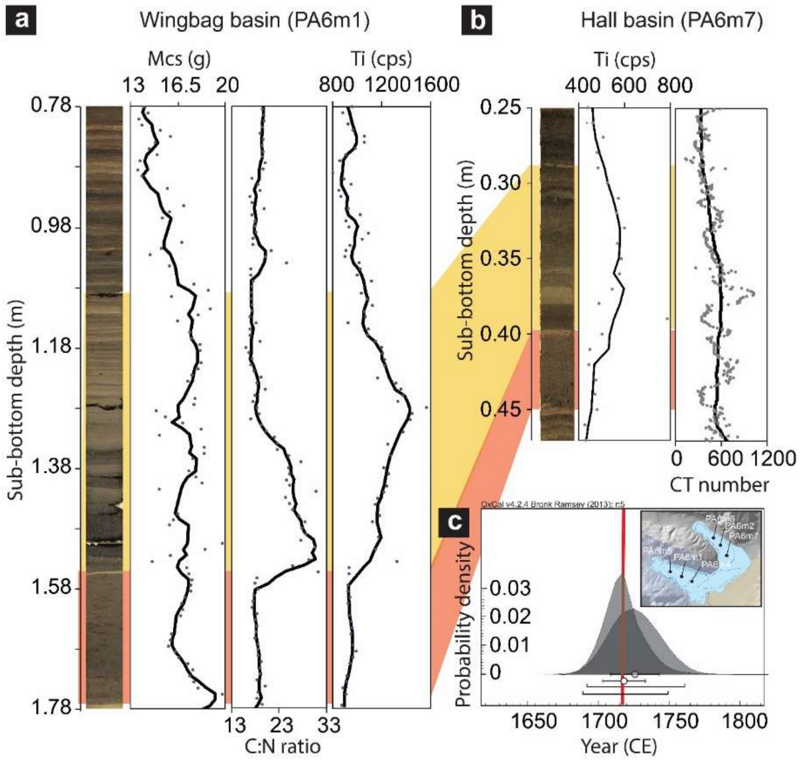

Supplementary Figure 2: Example showing the contrasting earthquake event sequences recording subaqueous mass-wasting and increased terrestrial sediment flux triggered by the 1717 CE Alpine Fault earthquake in the inflow proximal Windbag Basin and inflow distal Hall Basin of Lake Paringa. **a,** Core image, mass of clastic sediment, C:N ratios and normalised Ti counts per second (CPS), all independent proxies for terrestrial sediment flux, showing a type 2 RDL (orange) formed by subaqueous mass-wasting, overlain by a type 3 RDL stack (yellow) deposited by sequential hyperpycnal flows from the sediment laden influent rivers from PA6m1 in the Windbag Basin. **b,** Core image, Ti and CT number (a proxy for density) showing a type 2 RDL formed by subaqueous mass-wasting, overlain by a unit of L2 sediment formed by increased clastic sedimentation in the Hall Basin. **c,** Event age probability density functions showing the most recent earthquake deposits between basins in Lake Paringa correlate with the 1717 CE earthquake.

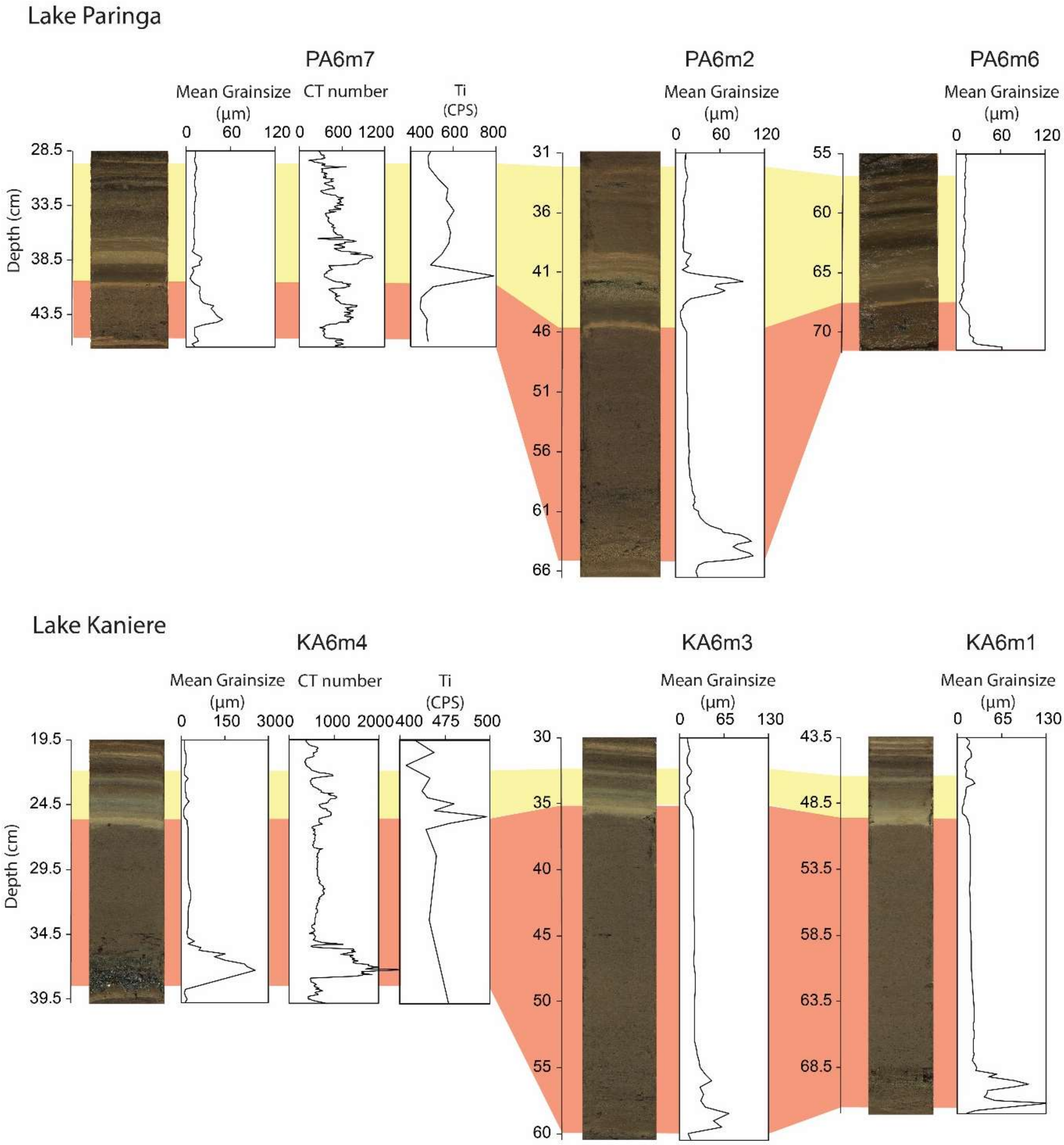

Supplementary Figure 3: Diagram showing examples of the earthquake event sequence formed in response to the 1717 CE earthquake in lakes Paringa and Kaniere, including digital image, CT tomography, mean grainsize, CT number and Ti concentration. Orange is the type 2 RDL, yellow is L2 dominated layered silt and white is L1 dominated layered silts.

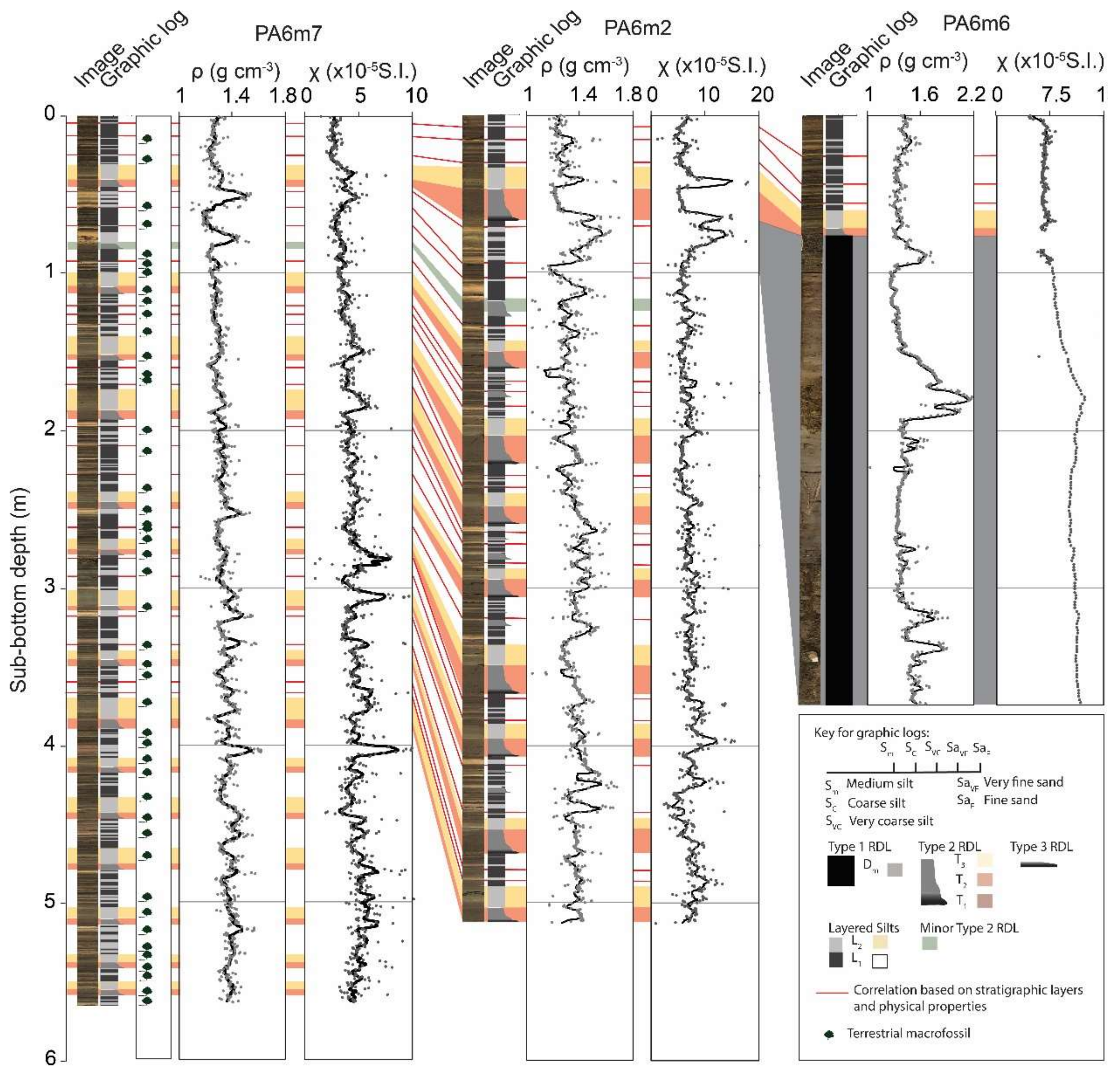

Supplementary Figure 4: Correlations between cores from Lake Paringa's Hall Basin showing core images, graphic logs, density (p) and magnetic susceptibility (χ). Grey - type 1 RDL, orange and yellow couplets –earthquake event sequences, and green - isolated type 2 RDL. Core site locations provided in source data file for Figure 1.

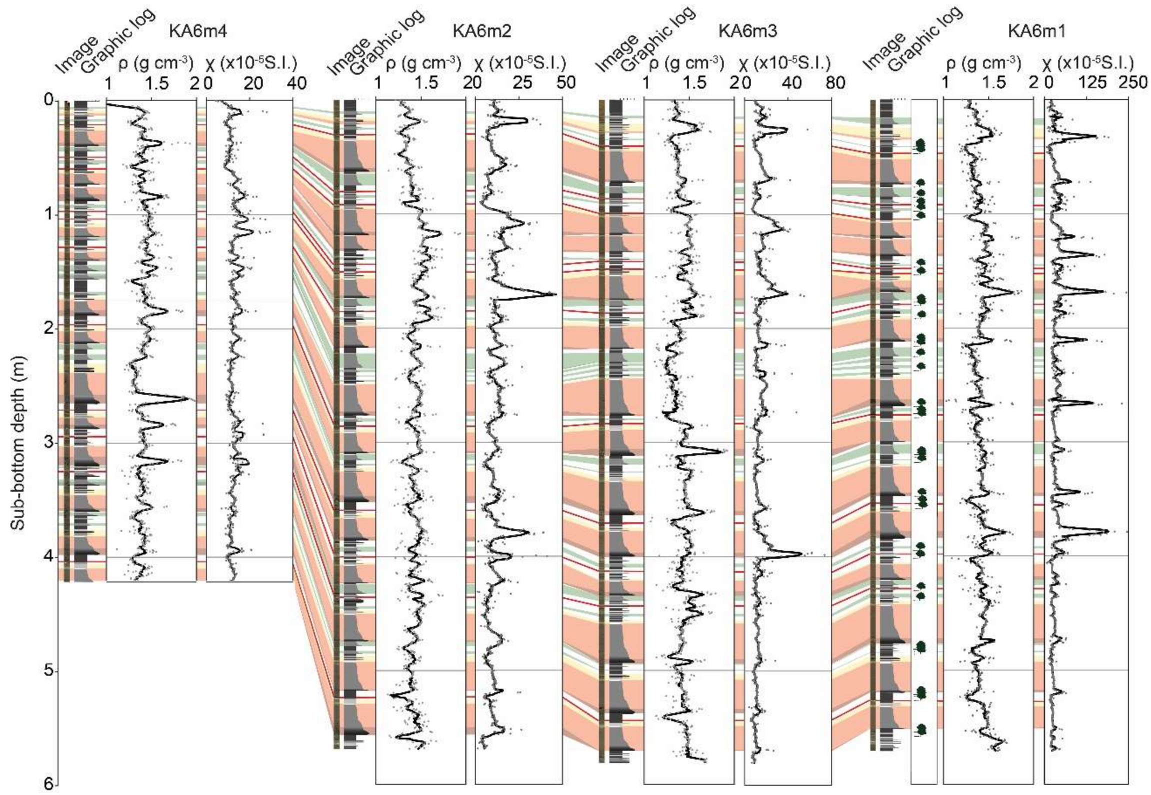

Supplementary Figure 5: Correlations between cores from Lake Kaniere showing core images, graphic logs, density (p) and magnetic susceptibility (χv). Grey - type 1 RDL, orange and yellow couplets – earthquake event sequences, and green - isolated type 2 RDL. See key for graphic logs in Supplementary Fig. 4. Core site locations provided in source data file for Figure 1.

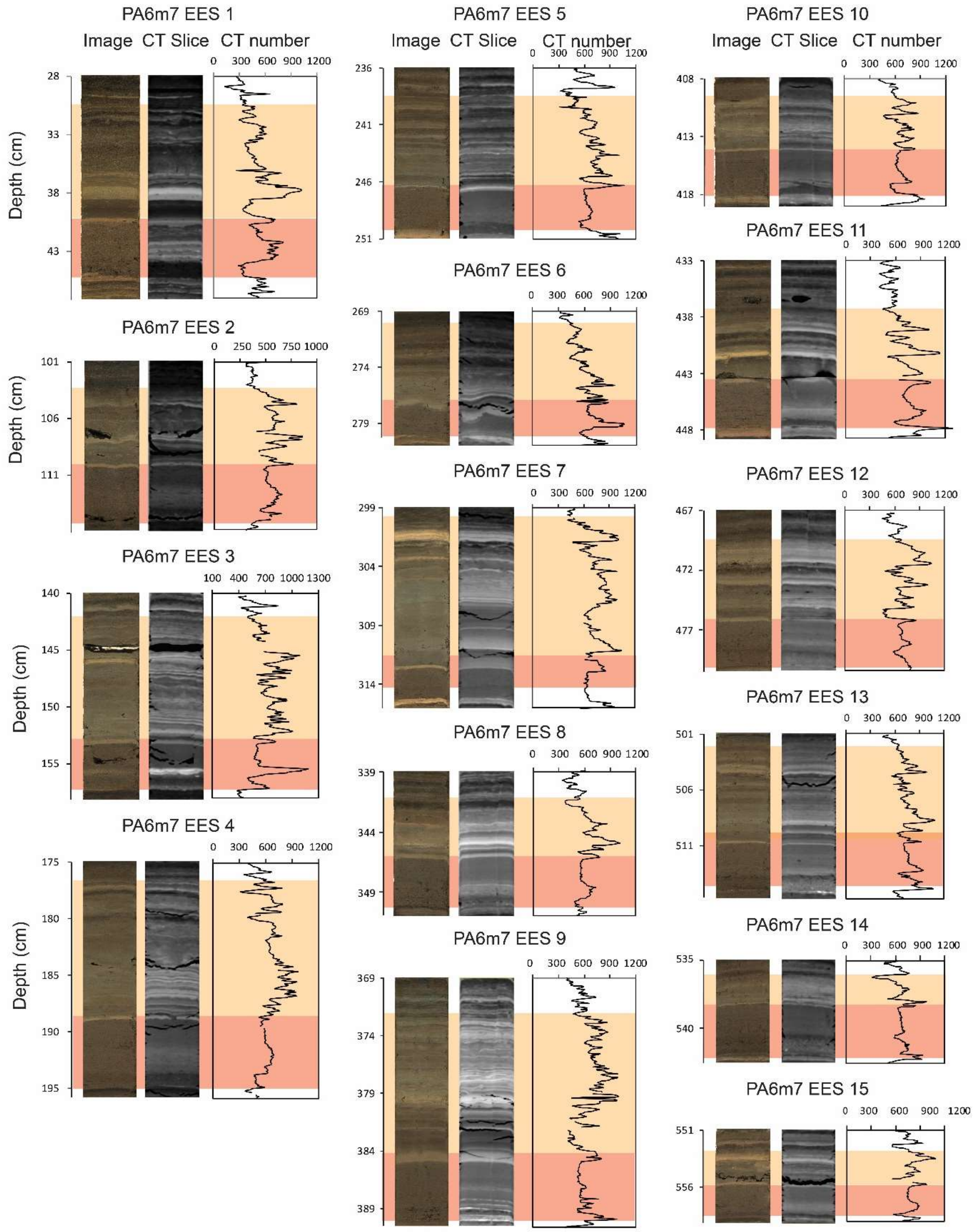

Supplementary Figure 6: Earthquake event sequences from the Hall Basin of Lake Paringa as recorded in core PA6m7 that show the core image, sagittal slice through the CT volume and CT number (a proxy for sediment density). In each case the type 2 RDL (orange) is overlain with L2 layered silts (yellow) demarked by a general increase in sediment density due to an increase of clastic sediments.

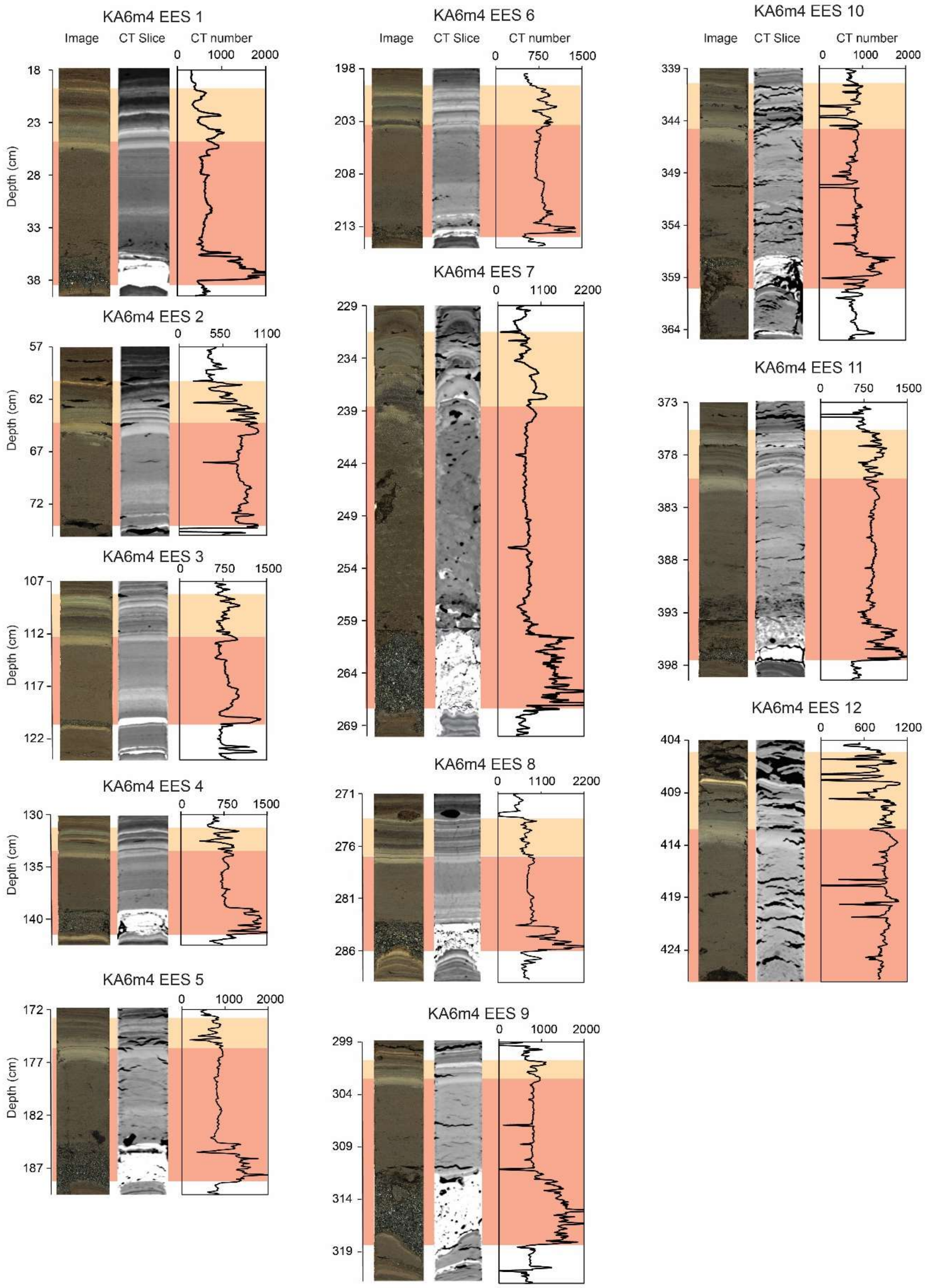

Supplementary Figure 7: Earthquake event sequences from Lake Kaniere as recorded in core KA6m4 that show the core image, sagittal slice through the CT volume and CT number (a proxy for sediment density). In each case the type 2 RDL (orange) is overlain with L2 layered silts (yellow) demarked by an increase in sediment density due to a general increase of clastic sediments.

Supplementary Discussion 2: developing an earthquake record of the central section

Developing a robust lacustrine paleoseismic record for the Central section requires EES to be dated precisely to facilitate inter-lake correlation. The 15 EES in Lake Paringa are constrained by 65 radiocarbon dates on terrestrial leaf macrofossils and small twigs that contain bark that have been isolated from intervals of layered silt (Supplementary Table 2). Core PA1 from the Windbag Basin recorded the last four EES[2,3], while 15 EES are recorded in core PA6m7 from the Hall Basin. P_Sequence age models for cores PA1 and PA6m7 were run concurrently with stratigraphically correlated EES made contingent between the two models for the last four events where the two cores overlap temporally. The resultant chronology has decadal precision (Supplementary Fig. 8) and an agreement index for the age model of 85% demonstrating acceptable fit between the modelled chronology and the un-modelled ^{14}C dates on which it is based[13]. This provides confidence that the chronology is accurate as well as precise. Ages for the earthquake event sequences are presented in Supplementary Table 3 as 95% highest probability density function (HPDF) ranges on the CE/BCE timescale.

Chronology for the 12 EES in the Lake Kaniere record was established using 37 terrestrial leaf or twig macrofossils isolated from intervals of layered silts (Supplementary Table 4). The age model based on the KA6m1 core stratigraphy provided event ages that generally have decadal precision (Supplementary Fig. 8). The agreement index of 76% is well above the 60% threshold for acceptable fit indicating the model accurately represents the modelled ^{14}C ages. Earthquake event sequence ages are reported in Supplementary Table 3.

The chronology for the Lake Mapourika record was also updated to better constrain ages for the most recent and fourth EES. Ages for these event sequences had been identified as under-constrained by radiocarbon dates in previous publications[1,2], raising concern about their accuracy. Here we present six new radiocarbon dates on terrestrial leaf macrofossils from the MA1 core stratigraphy (Supplementary Table 5). The updated P_sequence age model is constrained by 27 terrestrial leaf and small twig macrofossils, has an agreement index of 81%, well above the 60% threshold for acceptable fit, and provides event sequence ages that have decadal precision. The addition of six new ages to the Lake Mapourika chronology refines the ages for the most recent and fourth EES (Supplementary Table 3).

Ages for EES are correlated between all four lake sites where there is overlap in their temporal extent (Supplementary Table 3). Chi squared (χ^2) tests were used to test for a significant difference (α=0.05) in EES timing between the lakes. Results demonstrate that in all but one case there is no statistical difference between age PDFs for the last eight EES. We interpret this finding as evidence that, within error, subaqueous mass-wasting and increased sediment flux occurred synchronously at all four lake sites (Supplementary Discussion 3). The exception is the ~1150 CE EES where there is a significant difference between the event age PDFs from the lakes. However, the 95% HPDF ranges for all four lakes overlap and independent paleoseismic evidence for through-going rupture of the Central section at this time, supports a single event interpretation (Fig. 2, ref.[1]). Consequently, we interpret the ~1150 CE EES as recording the same event and attribute the poor temporal correlation to the inability of the age models to accommodate complexity in the radiocarbon calibration curve at this time (cf. ref.[1]). Limitations in record length mean that EES nine through 12 are only correlated between lakes Paringa and Kaniere and 13 through 15 are only recorded in Paringa.

Howarth et al.[1,2] argued that earthquakes were the only process capable of generating synchronous subaqueous mass-wasting and increased terrigenous sediment flux (i.e. EES) in two or more of the lake records. They also showed that EES form at Modified Mercalli Intensity (MMI) ≥ IX and can be used to map the spatial extent of MM IX shaking and hence fault rupture length when correlated temporally between sites. Turbidites that archive only subaqueous mass-wasting record lower shaking intensities of between MMI VI to VIII depending on the lake[1,2].

In addition to eliminating non-seismic trigger mechanisms it is also necessary to eliminate triggering by seismogenic sources other than the Alpine Fault. No active faults have been mapped in the central Southern Alps within 30 km of the central Alpine Fault[14]. However, while the Central section of the Alpine Fault accommodates up to 80% of the plate motion budget in the central South Island, the remaining motion is greater than that accounted for by geological slip rates on mapped active faults[15]. GPS velocities allow for up to 5 $mm.yr^{-1}$ of dextral fault-parallel deformation within a zone 100 km south east of the Alpine Fault[16]. The deficit can be explained by either uncertainty in the modeling of geodetic observations, the short timeframe of the geodetic observations, which may not accurately reflect long term rates of deformation, or accommodation of this deficit on unknown active faults within the high Southern Alps[17]. Cox et al.[15] identified 110 potentially active faults in the central Southern Alps within 60 km south east of the Alpine Fault. There is no paleoseismic evidence of Holocene displacements on these faults, although Cox et al. argue that erosion rates of up to 9 $mm.yr^{-1}$ (ref.[18]) may have obscured evidence of activity on these bedrock faults.

Howarth et al.[1] used isoseismal modelling of MMI shaking intensity to demonstrate that even synchronous rupture of these potentially active faults is not capable of generating the distribution of high intensity shaking reconstructed from the lakes. Their modelling also demonstrated that a M_w7.2 earthquake located immediately west of the Alpine Fault's surface trace under any of the lake sites could not produce the observed signal in the sedimentary record of multiple lakes. Near complete rupture of the Central section of the Alpine Fault is the only source capable of generating our observations. Hence, we are confident that EES correlated between multiple lakes provide a paleoseismic record of Alpine Fault ruptures. Shaking signatures recorded by subaqueous mass-wasting or EES that only occur in a single lake cannot be confidently attributed to the Alpine Fault[1] and so are not considered any further in this analysis unless they correlate with independent paleoseismic evidence. For example, subaqueous mass-wasting events in Lake Ellery that record shaking between MMI VII and IX and correlate temporally with independent evidence of rupture on the South Westland section are included in the analysis[1]. The single exception to this is EES14 in the Hall Basin of Lake Paringa, which we interpret as an Alpine Fault earthquake because it records MMI≥IX shaking at about the average inter-event time for Central section ruptures and no independent paleoseismic records for the Central section are long enough to corroborate it. Earthquake recurrence statistics generated from the Central section earthquake catalog are not sensitive to the inclusion (or not) of this event.

The lake-derived record of ruptures on the Alpine Fault offers an advantage over traditional paleoseismic approaches because the high sedimentation rate and continuous nature of the sedimentary archives mean they have the ability to distinguish shaking events closely space in time[1,9,19]. The occurrence of only a single turbidite formed by subaqueous mass-wasting in each EES from lakes Paringa and Mapourika points to a single shaking event on the central part of the Central section. A sequence of earthquakes would be recorded as two subaqueous mass-wasting derived turbidites with the clay caps of these units or only a few silt laminations preserved between them, which is not observed. Hence the lake records are consistent with single long ruptures rather than sequences of earthquakes that propagated along strike, such as those observed historically for the North Anatolian Fault[20].

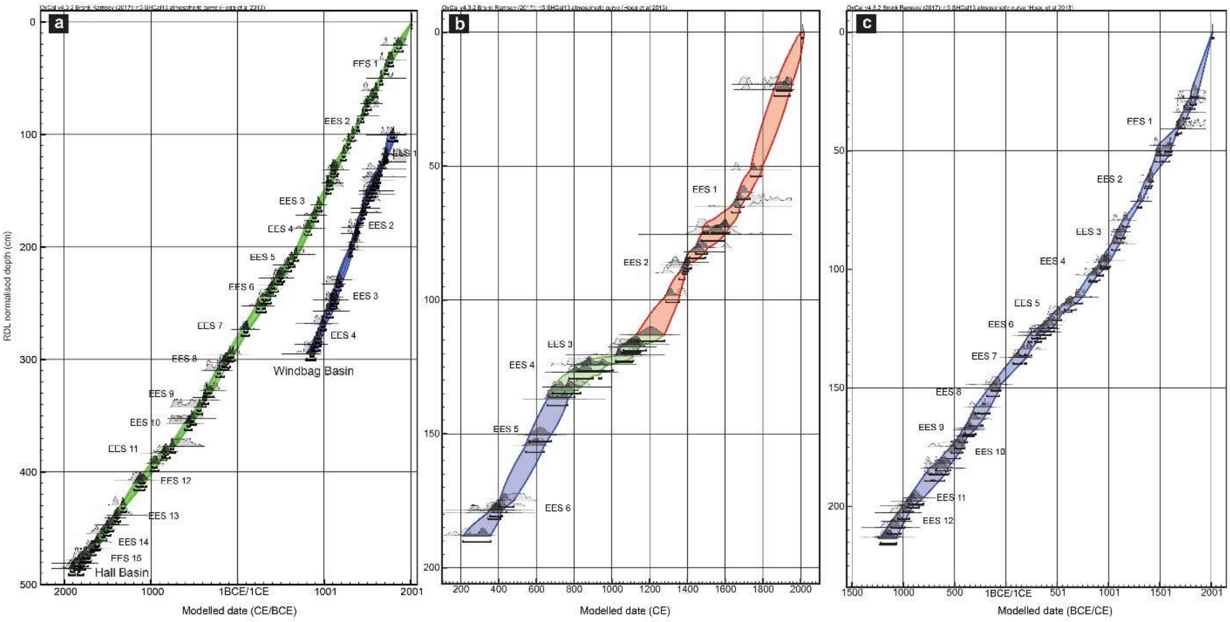

Supplementary Figure 8: Chronological models for the Hall Basin (based on core PA6m7) and Windbag Basin (based on PA1; ref.[2]) of Lake Paringa (**a**); Lake Mapourika based on core MA1[1] (**b**); and Lake Kaniere based core KA6m1 (**c**)**.** The age/depth models are based on the radiocarbon dates, the SHCal 13 calibration curve[21] and the P_sequence algorithm in OxCal 4.3 (ref.[22]), and show the calendar age likelihood (light grey) and posterior probability density functions (PDFs) (dark grey), as well as the age models at the 95% level of confidence. Rapidly deposited layer (RDL) normalised core depth is the depth of the core with rapidly deposited layers and voids removed.

Supplementary Table 2: Metadata for conventional radiocarbon ages (CRA) from the Hall Basin of Lake Paringa.

Depth [cm]	*RDL depth* [cm]	*Description*	*NZA*	*CRA* [yrBP]	*CRA error*	*d¹³C* [‰]	*d¹³C* error
17.3	17.8	*W. racemosa* leaf macrofossil that is well preserved	62206	135	21	-33.0	0.2
30.7	30.7	*W. racemosa* leaf macrofossil that is well preserved	62207	233	21	-30.6	0.2
61.0	50.2	*W. racemosa* leaf macrofossil that is well preserved	62208	259	22	-31.3	0.2
71.8	61.0	<1 mm twig macrofossil that is well preserved	62209	409	22	-28.9	0.2
91.5	72.4	Well preserved *W. racemosa* leaf macrofossil	OZR610	385	25	-29.8	0.1
95.0	75.9	Twig macrofossil	OZR606	410	20	-28.6	0.1
102.5	83.4	Well preserved *W. racemosa* leaf macrofossil	OZR607	485	20	-31	0.1
122.8	99.2	Unknown leaf macrofossil	OZO258	625	30		
129.8	105.3	Unknown leaf macrofossil	OZO259	775	30		
140.8	116.3	Unknown leaf macrofossil	OZO260	815	30		
157.7	130.6	Unknown leaf macrofossil	OZO261	935	30		
169.2	142.1	Combined twig and flower bud macrofossil	OZR609	1,020	20	-29.2	0.1
172.7	145.6	leaf macrofossil	OZO262	950	30		
204.0	170.6	Well preserved piece of a fern frond from an unknown taxa	OZR611	1,200	25	-28.5	0.1
217.4	182.4	Unknown leaf macrofossil	OZO264	1260	30		
239	205.3	Moderately well preserved *W. racemosa* leaf macrofossil	OZR612	1,350	25	-25.7	0.1
254.5	214.8	Well preserved *D. cupressinum* leaf macrofossil	OZR613	1,540	20	-27.1	0.1
263.5	223.8	Poorly preserved unknown broadleaf macrofossil	OZR614	1,605	25	-30.3	0.1
266.0	226.3	Combined leaf macrofossil from multiple spieces and a seed.	OZR615	1,615	25	-28.8	0.1
272.5	232.8	Well preserved *D. cupressinum* leaf macrofossil	OZR616	1,675	20	-27.1	0.1
285.5	243.1	Well preserved *D. cupressinum* leaf macrofossil	OZR617	1,735	30	-28.2	0.1
293.5	251.1	Well preserved *D. cupressinum* leaf macrofossil	OZR618	1,825	25	-28.7	0.2
315.8	270.5	Moderately well preserved partial unknown broadleaf macrofossil	OZR619	1,955	25	-29.7	0.1
340.5	292.8	Well preserved *D. cupressinum* leaf macrofossil	OZR621	2,075	25	-24.7	0.2
352.5	300.3	Poorly preserved partial unknown broadleaf macrofossil	OZR622	2,170	25	-29.4	0.1
359.3	307.1	Well preserved *D. cupressinum* leaf macrofossil	58286	2231	18	-29.6	0.2
377.5	324.6	Moderately well preserved partial unknown broadleaf macrofossil	OZR623	2,285	20	-27.7	0.1
395.5	336.6	Well preserved *D. cupressinum* leaf macrofossil	58287	2345	19	-27	0.2
402.2	342.7	Twig macrofossil with bark intact, <2 mm in diameter	58279	2492	18	-27.8	0.2
412.5	352.6	Moderately well preserved, partial *D. cupressinum* leaf macrofossil	58392	2444	22	-28.99	0.2

421.2	354.0	Poorly preserved *W. racemosa* leaf macrofossil	58280	2543	18	-32.9	0.2
436.3	372.2	Wood with bark macrofossil	58289	2518	18	-33.2	0.2
450.1	381.9	Well preserved *D. cupressinum* leaf macrofossil	58281	2794	19	-30	0.2
459.7	391.5	Well preserved *D. cupressinum* leaf macrofossil	58282	2855	19	-28	0.2
473.7	405.5	Well preserved *D. cupressinum* like macrofossil but may be macrophyte	58283	2984	19	-30.1	0.2
500.1	427.9	*L. scoparium* leaf, twig and flower macrofossils	58284	3166	18	-30.2	0.2
508.8	436.6	Well preserved, partial *D. cupressinum* leaf macrofossil	58393	3103	23	-29.9	0.2
520.4	445.2	Poorly preserved *W. racemosa* leaf macrofossil	58391	3231	20	-32.4	0.2
530.9	453.8	Poorly perserved unknown leaf macrofossil	62355	3375	20		
537.0	459.9	Well preserved Miro leaf macrofossil	62210	3339	26	-29.3	0.2
544.0	463.5	< 2 mm twig macrofossil	62211	3442	26	-29.64	0.2
549.6	469.1	Well preserved *D. cupressinum* leaf macrofossil	62212	3502	26	-30.75	0.2
559.8	476.1	Well preserved <2 mm diameter twig marofossil with flower heads an leaf that looks like Leptospermum	62213	3569	25	-26.3	0.2
564.4	480.7	Well preserved *D. cupressinum* leaf macrofossil	58039	3618	14	-30	0.2

Supplementary Table 3: Earthquake event sequence ages for lakes Ellery, Paringa, Mapourika and Kaniere, chi-squired test statistics for a difference in event age between sites and best estimate ages for ruptures of the Central section of the Alpine Fault.

Earthquake	*Lake Ellery* (CE/BCE)	*Lake Paringa* (CE/BCE)	*Lake Mapourika* (CE/BCE)	*Lake Kaniere* (CE/BCE)	***Chi squared test*	*Alpine Fault Central section earthquake age* (CE/BCE)
~1800				1809-1880		
1717	1681-1769	1693-1740	1668-1732	1685-1744	df=3; T=1.3; Tc=7.8; p>0.05	1696-1726
~1400	1365-1426	1370-1410	1386-1421	1362-1425	df=3; T=0.5; Tc=7.8; p>0.05	1386-1406
~1150*	1166-1213	1100-1180	1060-1183	1086-1171	df=3; T=10.3; Tc=7.8; p<0.05	1144-1180
	969-1022				N/A	
~950	916-991	915-981	822-1008	921-1006	df=3; T=2.6; Tc=7.8; p>0.05	936-978
~600	585-645	584-662	563-677	573-683	df=3; T=0.1; Tc=7.8; p>0.05	601-642
~400	329-430	330-437	353-420	345-475	df=3; T=0.9; Tc=7.8; p>0.05	373-413
~100	94-206	50-145		73-202	df=2; T=1.2; Tc=6.0; p>0.05	91-136
~-100	-148--18	-174--78		-181---66	df=2; T=0.7; Tc=6.0; p>0.05	-144--80
~-BCE300		-388--313		-410—291	df=1; T=0.1; Tc=3.8; p>0.05	-382--324
~-550		-592--498		-586--447	df=1; T=0.6; Tc=3.8; p>0.05	-569--495
~-800		-880--776		-949--803	df=1; T=1.9; Tc=3.8; p>0.05	-888--799
~-1100		-1188--1066		-1117—984	df=1; T=2.7; Tc=3.8; p>0.05	-1140--1050
~-1400		-1438--1362			N/A	-1436--1361
~-1600		-1696--1596			N/A	-1694--1594
~-1800		-1886--1770			N/A	-1884--1768

*Poor agreement between the event ages from the four lakes but interpreted as the same event based on the slip distribution for this event inferred from on-fault paleoseismic data (cf. ref. 1).

**df=degrees of freedom; T = χ^2 statistic; Tc= critical T χ^2 statistic; p = p value with alpha 0.05.

Supplementary Table 4: Metadata for conventional radiocarbon ages (CRA) from Lake Kaniere.

Depth [cm]	*RDL depth* [cm]	*Description*	*NZA*	*CRA* [yrBP]	*CRA error*	*d^13^C* [‰]	*d^13^C* error
38.9	27.9	Well preserved *Podocarpus totora* leaf macrofossil	58394	164	15	-26.9	0.2
40.9	29.9	Well preserved *D. cupressinum* leaf macrofossil	56506	178	20	-28.64	0.2
44.8	33.7	Well preserved, partial *D. cupressinum* leaf macrofossil	58395	210	15	-29.8	0.2
80.8	39.9	Well preserved, partial *Metrosideros spp*. leaf macrofossil	58396	164	15	-28.8	0.2
83.5	40.7	Twig macrofossil with bark intact, <2 mm in diameter	58285	240	16	-26.7	0.2
90.1	47.7	Well preserved partial *D. cupressinum* leaf macrofossil	56528	442	21	-32.57	N/A
95.1	52.0	Moderately preserved unknown broadleaf leaf macrofossil	56529	407	21	-35.32	N/A
103.5	60.4	Well preserved *D. cupressinum* leaf macrofossil	57516	578	23	-29.01	0.2
144.3	71.3	Well preserved unknown broadleaf leaf macrofossil and two *D. cupressinum* spurs	57517	703	23	-26.39	0.2
152.3	79.3	Unknown broadleaf macrofossil, moderate to poor preservation	56463	949	18	-29.83	0.2
177.2	86.2	Moderately well preserved *P. totora* leaf attached to twig	57518	984	23	-27.55	0.2
180.2	89.2	Well preserved *D. cupressinum* leaf macrofossil	57519	975	23	-29.58	0.2
191.5	96.2	Well preserved unknown broadleaf macrofossil and flower head	57520	1100	24	-30.44	0.2
211.4	97.3	Well preserved *D. cupressinum* leaf macrofossil	57521	1184	24	-29.32	0.2
214.2	100.1	*W. racemosa*, well preserved	56464	1157	18	-32.96	0.2
225.0	102.7	Moderately well preserved unknown broadleaf macrofossil	57522	1266	24	-28.66	0.2
237.0	111.7	Moderately preserved unknown broadleaf leaf macrofossil	56530	1325	21	-27.01	0.2
268.3	115.3	Poorly preserved unknown broadleaf leaf fragment	56679	1513	25	-34.74	N/A
274.8	118.9	Moderately preserved unknown broadleaf leaf macrofossil	56531	1628	21	-29.06	0.2
277.8	121.9	Well preserved *D. cupressinum* leaf macrofossil	57523	1633	24	-28.62	0.2
308.5	126.5	Moderately preserved W. *racemosa* leaf macrofossil	57515	1746	24	-28.67	0.2
310.0	128.0	Well preserved *D. cupressinum* leaf macrofossil	56532	1830	21	-30.04	0.2
315.7	133.7	Well preserved partial *D. cupressinum* leaf macrofossil	56533	1841	21	-29.49	0.2
344.4	137.1	Well preserved partial *D. cupressinum* leaf macrofossil	57586	1932	16	-28.69	0.2
355.8	148.6	Poorly preserved unknown broadleaf leaf macrofossil	56678	2131	26	-31.08	N/A
391.3	158.2	Moderately preserved *W. racemosa* leaf macrofossil	57587	2206	17	-31.69	0.2
398.3	163.4	Moderately well preserved unknown broadleaf macrofossil	57588	2222	17	-28.24	0.2
429.6	170.4	Well preserved *D. cupressinum* leaf macrofossil	57589	2385	17	-28.16	0.2
438.8	174.8	Poorly preserved broadleaf macrofossil and three flower heads	57590	2456	18	-29.28	N/A
481.5	182.2	Moderately well preserved *P. totara* leaf macrofossil	57591	2555	18	-30.22	0.2

483.2	183.9	Well preserved partial *D. cupressinum* leaf macrofossil	56526	2549	21	-28.03	0.2
485.9	186.6	Partial *D. cupressinum* leaf macrofossil	57592	2575	18	-31.26	N/A
524.7	197.9	Broad leaf fragment	57593	2791	18	-26.61	0.2
526.4	199.6	Moderately well preserved *D. cupressinium* fragment	57594	2860	18	-29.72	0.2
529.4	202.6	Well preserved *D. cupressinum* leaf macrofossil	57595	2909	18	-30.41	0.2
556.2	208.9	Unknown broadleaf macrofossil, moderate well preserved	56465	2955	21	-26.49	0.2
560.3	213	Poorly preserved unknown broadleaf leaf macrofossil	56527	2986	23	-30.52	0.2

Supplementary Table 5: Metadata for conventional radiocarbon ages (CRA) from Lake Mapourika.

Depth [cm]	*RDL depth* [cm]	*Description*	*NZA*	*CRA* [yrBP]	*CRA error*	*d[13]C* [‰]	*d[13]C* error
19.5	19.5	*W. racemosa* leaf	NZA62225	163	22	-28.6	0.2
21.4	21.4	*W. racemosa* leaf	NZA62219	130	21	-31.7	0.2
	51.5	*D. cupressinum* leaf	NZA63206	257	19	-29.6	0.2
120	63	Unknown leaf	OZN516	195	30	-30.2	0.1
122	65	Unknown leaf	OZM929	265	30	-28.5	0.1
132	72.5	Unknown leaf	OZM944	420	25	-29.8	0.1
137	75.5	Unknown leaf	OZM945	410	100	-25	
162	80.5	Unknown leaf	OZN512	430	30	-31.1	0.1
216	86	*W. racemosa* leaf	OZL515	620	25	-28.1	0.1
217	87	Twig	OZM926	640	30	-24.8	
219	88	Unknown leaf	NZA63047	656	20	-27.82	0.2
221	90	*D. cupressinum* leaf	OZM950	745	30	-28.2	0.1
244	98.5	*D. cupressinum* leaf	OZN522	695	30	-30.6	0.2
278	117.5	*D. cupressinum* leaf	OZM946	1035	30	-31.6	0.4
278.5	106.5	D. cupressinum leaf	NZA63205	977	19	-30.5	0.2
282	120.5	Unknown leaf	OZM954	1060	45	-32.6	0.1
282.5	121.0	*P. Totara* leaf	NZA63048	1003	20	-27.92	0.2
303	124.5	Unknown leaf	OZM930	1260	35	-28.4	0.4
309	127.0	Unknown leaf	OZM927	1230	30	-26.1	0.1
314	132.5	Unknown leaf	OZN523	1285	30	-30.4	0.1
32	137.0	*D. cupressinum* leaf	OZN524	1370	35	-29	0.1
3.99	154.5	Unknown seed	OZM955	1510	35	-24.8	0.1
4.29	175.0	*D. dacrydioides* leaf	OZM956	1605	30	-28.8	0.1
4.31	177.0	*W. racemosa* leaf	OZM949	1675	35	-31.6	0.1
5.15	178.5	Unknown leaf	OZL543	1735	30	-27.7	0.2
5.16	179.5	*D. cupressinum* leaf	OZM957	1730	35	-28.8	0.1
5.42	188	Unknown leaf	OZM931	1835	35	-28.8	0.1

Supplementary Discussion 3: distinguishing single and multi-section ruptures

To reconstruct the spatial pattern of rupture along the Central and South Westland sections of the Alpine Fault we compare the lacustrine paleoseismology record from the Central section developed here with previously published paleoseismic records from two fault-bounded swamp sites that provide the timing of surface rupturing earthquakes (M_w>7) on the South Westland section[23,24]. Alpine Fault earthquakes are recorded in the stratigraphy of the swamps as transitions between peat and silt units because large displacements during earthquakes (~7.5 m dextral and ~1 m west-side up) impound rivers draining across the fault causing water to pond against the scarp[23,24]. Evidence for both synchronous and independent ruptures of the Central and South Westland sections was revealed by combining statistical comparison of earthquake ages between sections using χ^2 tests (α = 0.05) with details of the shaking signatures preserved in the lakes and published earthquake signature confidence ranks[24] (Methods; Supplementary Table 6). Earthquake signature confidence at the John O'Groats (JOG) site is based on the prominence and spatial extent of peat-silt transitions in this wetland. Lower event confidence has previously been interpreted to represent reduced surface displacement and hence disruption of the river crossing the scarp at this locations[24].

During the last 2500 years where earthquake data exists at the majority of sites, the record demonstrates the fault has switched between modes of ruptures that either pass or terminate in the vicinity of the Central-South Westland (C-SW) section boundary. For example, three ruptures are inferred to have spanned the section boundary as multi-section earthquakes between ~1730 CE and ~1100 CE, because there is no significant difference between earthquake ages (Supplementary Table 6). The multi-section rupture interpretation is supported by the large single event displacements on the fault[25], single EES in lakes Mapourika, Paringa and Ellery, and the very high to high earthquake signature rankings at the JOG site (Fig. 2a,b, c), all of which are indicative of through going rupture similar to the 1717 CE earthquake[26,27].

Between ~900 CE and ~300 CE ruptures were most likely confined to single-sections because either: 1) there are significant differences in ages between Central and South Westland section earthquakes; 2) earthquakes on the South Westland section correlate with shaking deposits in Lake Ellery formed by between MMI VII to IX indicating a decrease in shaking north of their rupture tip; and/or 3) the strength of the event signatures in the JOG wetland suggests these events terminated in the vicinity of the section boundary. The ~900 CE Central, ~800 CE South Westland and ~700 CE South Westland section ruptures are inferred to be single section ruptures because there are significant differences ($p<0.05$) between event age PDFs between the sections (in fact there is no overlap between the 95% HPDF ranges of the event ages; Fig. 2c; Supplementary Table 6). The location of Lake Ellery near the C-SW section boundary makes the site uniquely placed to record sedimentary evidence of ruptures that terminate close enough to the lake to produce ground motions of MMI>VII, which is the recording threshold for the lake[1]. Howarth et al.[1] show that a shaking event of between MMI VII and IX occurred at the Lake Ellery at 845–773 CE and may record the termination of the ~800 CE rupture of the South Westland section. The lack of a shaking signature in Lake Ellery for the ~700 CE South Westland section earthquake may suggest the rupture terminated at a more southern location than the ~800 CE earthquake[1]. Alternatively, as rupture directivity influences the spatial distribution of MMI VI to VIII shaking away from rupture tips on the Alpine Fault[28], the ~700 CE South Westland section rupture may have had a northern hypocenter and north to south directivity, limiting the spatial extent of shaking north of the rupture. Terminating ruptures that produce less slip at the Hokuri Ck. and JOG sites are also consistent with the earthquake signature confidence only being moderate for those events at JOG (where the peat-silt transitions were ranked according to their strength) compared to the signatures of the through-going ruptures between 1730 CE and 1100 CE.

The ~600 CE and ~400 CE Central section ruptures both overlap with the broad age PDF for the ~500 CE rupture on the South Westland section (Fig. 2c; Supplementary Table 6). Based on temporal correlation alone, at least one of the Central section earthquakes must be confined to the Central section, while the other could be interpreted as a multi-section rupture based on temporal correlation with the South Westland section rupture. However, we argue all three of these earthquakes are most likely single section ruptures based on event signature strength at JOG and the absence of event evidence at Hokuri Ck[24,29]. The 500 CE event is not recorded at Hokuri Ck. and has the lowest possible confidence ranking at JOG. The weakness of the peat-silt transition may suggest slip at JOG was much reduced compared to the other earthquakes recorded there and hence unlikely to be a through-going rupture with large surface displacement[24]. The age PDF for the ~500 CE South Westland section rupture also has the most overlap with a shaking event between MMI VII and IX in Lake Ellery that may record shaking from a single section rupture that terminated near the JOG site but had south to north directivity, producing a lobe of MMI VII shaking intensity north of the rupture tip. Hence, the most parsimonious interpretation remains a sequence of three single section ruptures between 600 CE and 400 CE, acknowledging that there is a greater degree of uncertainty in the interpretation due to the overlapping earthquake age PDFs.

The ~300 CE earthquake on the South Westland section has no correlate in the Central section record and is also inferred to be a single section rupture[24]. Following previously published interpretations we infer this JOG event is distinct from the ~100 CE earthquake at Hokuri Ck. despite the 8 year overlap in the 95% HPDF ranges[23].

No statistical difference in earthquake ages between the two sections between ~300 CE and ~400 BCE indicates that three ruptures most likely propagated through the section boundary producing a mode of three multi-section earthquakes (Fig. 2c). The interpretation is supported by single EES in lakes Paringa and Ellery. Between ~500 BCE and ~2000 BCE, the spatial completeness of the paleoseismic record decreases substantially, making it difficult to determine precisely where ruptures terminate during this period. However, 43% of earthquakes within this time period appear to be limited to either the Central or South Westland sections in a pattern of alternating passing and terminating ruptures (Fig. 2c; Supplementary Table 6).

Supplementary Table 6: Statistical comparison between earthquake ages from the Central and South Westland sections used to define terminating and through-going ruptures.

Alpine Fault Earthquake (CE/BCE)	*Central EQ age* (CE/BCE)	*MMI between VII and IX shaking in Lake Ellery**	*South Westland EQ age*** (CE/BCE)	****Chi Squared test*	Best Estimate Alpine Fault Earthquake Age (CE/BCE)
	No rupture	1871-1962	No rupture	No potential correlate	
1717	1696-1726		1705-1775	df=1; T=2.7; Tc=3.8; p>0.05	1701-1732
	No rupture	1524-1597	No rupture	No potential correlate	
~1400	1386-1406		1335-1394	df=1; T=3.0; Tc=3.8; p>0.05	1384-1400
~1150	1144-1180		1104-1205	df=1; T=0.2; Tc=3.8; p>0.05	1148-1179
~950	936-978		No rupture	No potential correlate	936-978
~800	No rupture	759-860	782-902	df=1; T=0.7; Tc=3.8; p>0.05	782-902
~700	No rupture		655-739	No potential correlate	655-739
~600	601-642		?	df=1; T=1.4; Tc=3.8; p>0.05	601-642
~500	?	364-448	396-626	df=1; T=0.4; Tc=3.8; p>0.05	396-626
~400	373-413		?	df=1; T=1.2; Tc=3.8; p>0.05	373-413
~250	No Rupture		223–319	No potential correlate	223–319
~100	91-136		111-232	df=1; T=3.5; Tc=3.8; p>0.05	94-194
~-100	-144--80		-259--72	df=1; T=1.9; Tc=3.8; p>0.05	-149--87
~-350	-382--324		-494--294	df=1; T=2.2; Tc=3.8; p>0.05	-387--330
~-550	-569--495		No rupture	No potential correlate	-569--495
~-800	-888--799		-851--771	df=1; T=2.6; Tc=3.8; p>0.05	-854--789
~-950	No rupture		-1000--909	No potential correlate	-1000--909
~-1100	-1140--1050		No rupture	No potential correlate	-1144--1053
~-1400	-1436--1361		-1450--1270	df=1; T=0.2; Tc=3.8; p>0.05	-1428-1360
~-1600	-1694--1594		No rupture	df=1; T=5.0; Tc=3.8; p<0.05	-1684--1588
~-1800	-1884--1768		-1831--1650	df=1; T=1.0/Tc=3.8; p>0.05	-1830--1650

*from Howarth et al. (ref.[1])

**from Cochran et al. (ref.[24])

**df=degrees of freedom; T = χ^2 statistic; Tc= critical T χ^2 statistic; p = p value with alpha 0.05.

***No potential correlate - the 95% HPDF range for earthquake ages on adjacent sections does not overlap precluding the need for a χ^2 test.

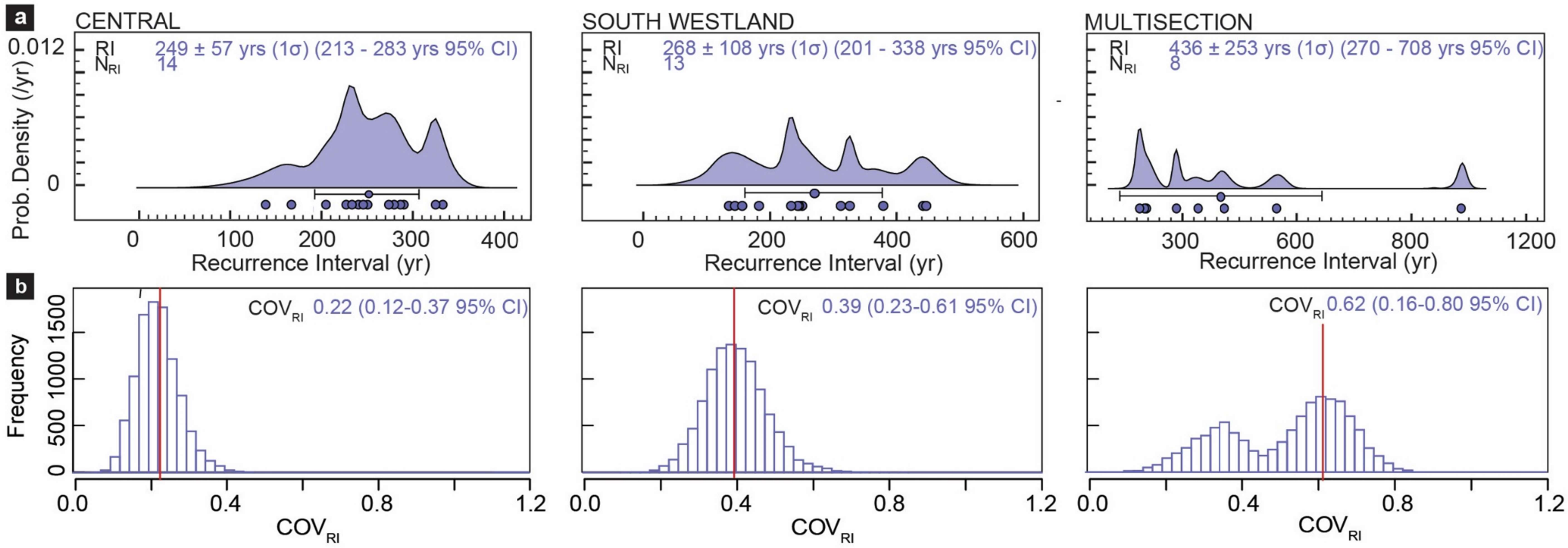

Supplementary Figure 9: Earthquake recurrence statistics derived from the paleoseismic record. **a,** Summed recurrence interval distributions for rupture of the Central, South Westland and multi-section ruptures. **b,** Frequency histograms for the coefficients of variation (σ/μ) for the recurrence intervals (COV_{RI}). Circles in part **a** present the individual inter-event times between earthquakes.

1.4 Supplementary Discussion 4: implications of loading simulations with backslip

Stressing rates that drive the simulations were calculated using the backslip method[30] based on geologically derived long-term slip rates[31,32,33] and applied to each element at the assigned rake angle. The backslip calculation is used to derive the external loading of RSQSim because in an elastic medium the long-term average stressing rate must be accommodated by long term average slip on the fault(s) to avoid stresses trending towards infinity. Put another way, if the geometry of the explicitly modeled fault(s) is well represented by the fault model, and if the fault elements do indeed slip at the prescribed rates, then over the long-term the average stressing rate must be zero. Loading the model using backslip is equivalent to loading the fault by far field tectonic displacement (a forward model) if the fault is vertical, strike-slip, and aligned with the far-field tectonic motions. However, backslip and far-field displacement loading result in differences in stress loading when fault geometries are more complex. Here we discuss the most appropriate approach for loading multi-cycle simulations of the Alpine Fault.

The Alpine Fault is modelled as a single through-going surface. Due to this, changes in strike, dip and seismogenic depth at the C-SW section boundary are accommodated at depth by a releasing bend followed by a restraining bend (from south to north through the section boundary; Fig. 1b). When fault elements to the south and north of these bends slip, extensional normal stress is transferred to the releasing bend and compressive normal stress to the restraining bend in both the backslip and far-field displacement loaded cases. However, the inter-seismic stressing rates for the two loading approaches have the opposite sign. Backslip loads the releasing bend with compressive inter-seismic stresses, while far-field displacement loading results in compressive stresses. The reverse is true for the restraining bend.

To understand the implications of the difference between backslip and far-field displacement loading approaches it is important to consider their implications over the long-term. In the case of the releasing bend, loading by far-field displacement causes both the driving stresses and those from fault slip to be extensional. In the long term, this results in ever decreasing normal stress to the point where the slip behaviour approaches continuous creep and/or fault normal opening occurs. For the restraining bend the opposite is true, both the driving stresses and those from slip are compressive resulting in increasing normal stress and a fault section that does not slip. Both scenarios that arise from far-field displacement loading are unrealistic in the case of the C-SW section boundary on the Alpine Fault because Quaternary geology shows: 1) a well expressed through-going surface trace that offsets late Holocene geomorphic features[33,34]; 2) evidence of large single event displacements at the surface for the last three events of 8-9 m[25,35]; 3) that both the degree of trace expression and single event displacements magnitude in the boundary region are equivalent to those on the fault sections to the north and south, and 4) there is no evidence of aseismic creep at the surface anywhere in the boundary region[34].

By loading the model using backslip we indirectly account for inter-seismic processes such as non-elastic effects (e.g. visco-elastic relaxation) or slip on small unmodelled dip-slip faults in the boundary region that alter normal stresses at the fault bends allowing them to slip in earthquakes. We deem this behavior more appropriate than the simple far-field displacement loading but acknowledge that our model is a very simplified approximation of the physics of real world faults. Fully dynamic multi-seismic cycle simulations with realistic non-elastic rheology loaded by far-field tectonic displacements and not subject to the limitations of RSQSim approximations would be preferable but would be too computationally expensive to run on realistic 3D geometries. Nonetheless, the agreement between the emergent model behavior and the paleoseismic record provides some confidence that the RSQSim simulations are representative of the real world Alpine Fault, though we acknowledge our conclusions on the mechanisms driving mode-switching are tentative.

Supplementary Table 7: Full parameterization for the Realistic Alpine Fault geometry model, Alpine Fault strike and seismogenic dip model, Alpine Fault strike model and the Planar fault model.

Parameterization of Alpine Fault RSQSim models	**Model Parameters**	**Dusky to Caswell**	**Caswell to Milford**	**Milford to Martyr**	**Martyr to Haast**	**Haast to Toaroha**	**Toaroha to Maruia**	**Maruia to Makakitaki**	**Matakitaki to Cook Strait**
	Avg Upper Seis Depth (km)	0	0	0	0	0	0	0	0
Realistic Alpine Fault geometry	Avg Lower Seis Depth (km)	15	15	15	15	8	15	15	15
	Avg Dip (degrees)	80	82	82	46	45	60	65	85
	Avg Dip Direction (azimuth)	131	143	141	149	247	146	102	157
	Avg Long Term Slip Rate (mm/yr)	31.4	27.2	28	28	28	12	6	3
	Avg Seismic Slip Factor	0	0	0	0	0	0	0	0
	Avg Rake	-175	-175	-172	138	138	127	110	-175
	Normal Stress (MPa)	184	184	184	184	184	184	184	184
	(b-a)	0.007	0.007	0.007	0.007	0.007	0.007	0.007	0.007
	Number of Surface Trace Points Used	4	4	8	6	8	6	10	19
	Trace Length (derivative value, in km)	128	99	73	49	202	115	38	151
	Thickness of creeping zone beneath seis zone (km)	15	15	15	15	8	15	15	15
	Summary	Realistic geometry and kinematics largely as compiled in Barth et al. (2013)							
	Avg Upper Seis Depth (km)	0	0	0	0	0	0	0	0
	Avg Lower Seis Depth (km)	15	15	15	15	8	15	15	15

Alpine Fault strike and seismogenic depth	Avg Dip (degrees)	90	90	90	90	90	90	90	90
	Avg Dip Direction (azimuth)	131	143	141	149	247	146	102	157
	Avg Long Term Slip Rate (mm/yr)	31.4	27.2	28	28	28	12	6	3
	Avg Seismic Slip Factor	0	0	0	0	0	0	0	0
	Avg Rake	-175	-175	-172	138	138	127	110	-175
	Normal Stress (MPa)	184	184	184	184	184	184	184	184
	(b-a)	0.007	0.007	0.007	0.007	0.007	0.007	0.007	0.007
	Number of Surface Trace Points Used	4	4	8	6	8	6	10	19
	Trace Length (derivative value, in km)	128	99	73	49	202	115	38	151
	Thickness of creeping zone beneath seis zone (km)	15	15	15	15	8	15	15	15
	Summary	Realistic kinematics, strike, seismogenic depth but vertical dip							
Alpine Fault	Avg Upper Seis Depth (km)	0	0	0	0	0	0	0	0
	Avg Lower Seis Depth (km)	15	15	15	15	15	15	15	15
	Avg Dip (degrees)	90	90	90	90	90	90	90	90
	Avg Dip Direction (azimuth)	131	143	141	149	247	146	102	157
	Avg Long Term Slip Rate (mm/yr)	31.4	27.2	28	28	28	12	6	3
	Avg Seismic Slip Factor	0	0	0	0	0	0	0	0
	Avg Rake	-175	-175	-172	138	138	127	110	-175

Strike	Normal Stress (MPa)	184	184	184	184	184	184	184	184
	(b-a)	0.007	0.007	0.007	0.007	0.007	0.007	0.007	0.007
	Number of Surface Trace Points Used	4	4	8	6	8	6	10	19
	Trace Length (derivative value, in km)	128	99	73	49	202	115	38	151
	Thickness of creeping zone beneath seis zone (km)	15	15	15	15	8	15	15	15
	Summary	Realistic kinematics and strike but constant seismogenic depth and vertical dip							
Planar fault	Avg Upper Seis Depth (km)	0	0	0	0	0	0	0	0
	Avg Lower Seis Depth (km)	15	15	15	15	15	15	15	15
	Avg Dip (degrees)	90	90	90	90	90	90	90	90
	Avg Dip Direction (azimuth)	n/a	n/a	n/a	n/a	n/a	n/a	n/a	n/a
	Avg Long Term Slip Rate (mm/yr)	31.4	27.2	28	28	28	12	6	3
	Avg Seismic Slip Factor	0	0	0	0	0	0	0	0
	Avg Rake	-175	-175	-172	138	138	127	110	-175
	Normal Stress (MPa)	184	184	184	184	184	184	184	184
	(b-a)	0.007	0.007	0.007	0.007	0.007	0.007	0.007	0.007
	Number of Surface Trace Points Used	1	0	0	0	0	0	0	1
	Trace Length (derivative value, in km)	126	98	73	49	201	115	33	146

	Thickness of creeping zone beneath seis zone (km)	15	15	15	15	15	15	15	15
	Summary	Realistic kinematics as above but with a planar vertical fault with uniform seismogenic depth							

Supplementary Table 8: The fraction of time that simulated event fractions, mean RIs, and COV_{RI} from the 4-kyr running windows are within tolerances of paleoseismic values (95% CI for other statistics). As there are only single values for paleoseismically derived event fractions we can only report whether that value falls within the distribution of simulated values.

	Multi	Central only	South only	Central mean RI	Central RI COV	South mean RI	South RI COV	Multi mean RI	Multi RI COV
Planar fault 33 kyr	No	No	No	0.37	0.56	1.00	0.00	0.43	0.32
Alpine Fault strike 33 kyr	No	No	Yes	0.62	0.44	1.00	0.00	0.54	0.22
Alpine Fault strike and depth 33 kyr	No	No	Yes	0.95	0.16	0.90	0.28	0.40	0.60
Realistic Alpine Fault geometry 33 kyr	Yes	Yes	Yes	0.53	0.27	1.00	0.16	0.58	0.40
Realistic Alpine Fault geometry 100 kyr	Yes	Yes	Yes	0.44	0.34	0.95	0.34	0.51	0.33

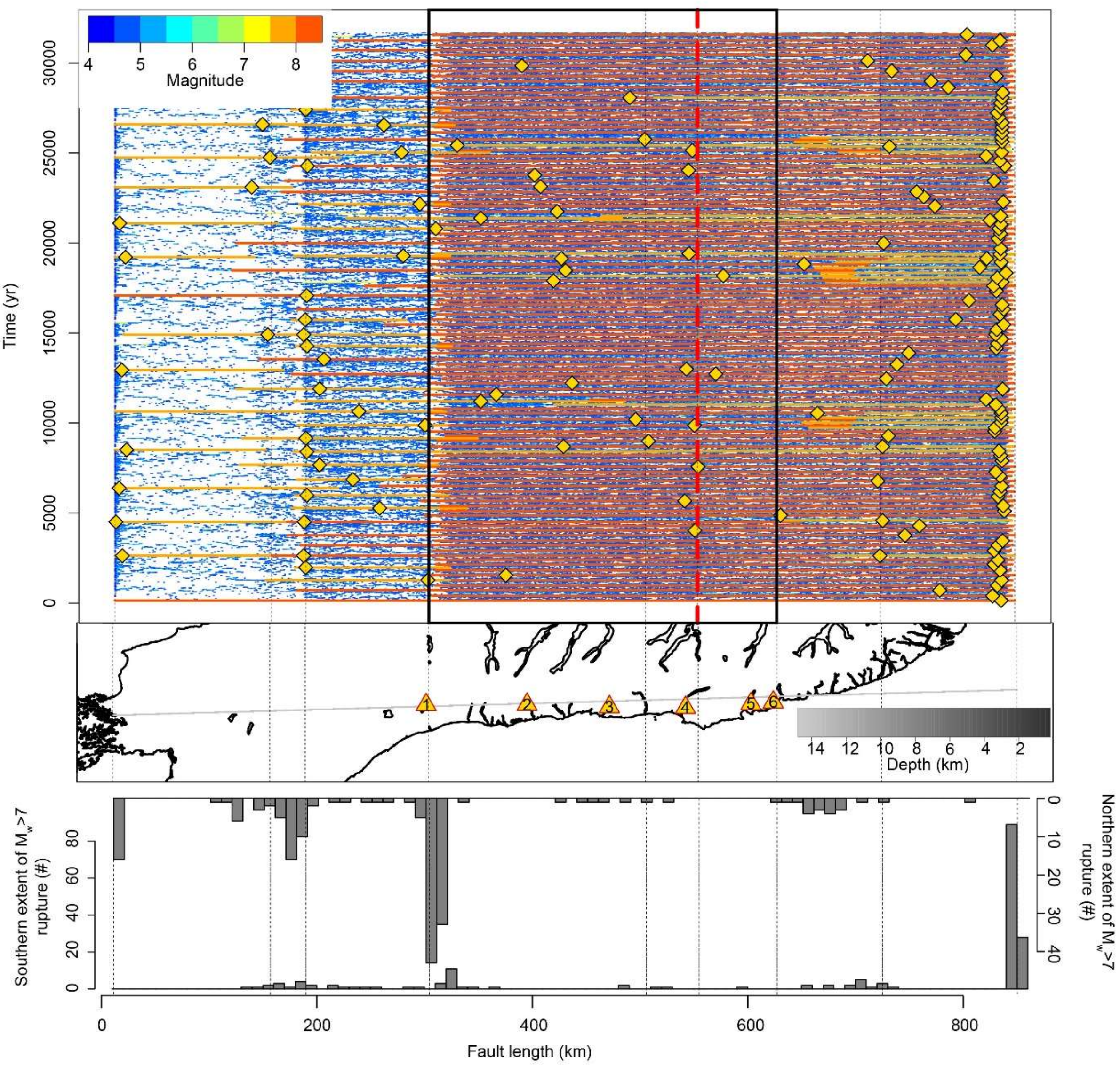

Supplementary Figure 10: Complete earthquake catalog (M_w>4) for the 33 kyr RSQSim Planar fault simulation (realistic kinematics, constant strike, seismogenic depth, vertical dip and homogeneous friction parameters). The black rectangle demarks the spatial extent of the paleoseismic data and the vertical red dashed line represents the location of the boundary between the Central and South Westland fault sections. Yellow diamonds indicate the epicenters of M_w>7 earthquakes. Numbered triangles in the middle panel show the location of the paleoseismic sites used in this study: 1) L. Kaniere, 2) L. Mapourika, 3) L. Paringa, 4) L. Ellery, 5) Hokuri Ck., and 6) John O'Groats R. The bottom panel shows the location and number of rupture terminations for earthquakes with M_w>7.

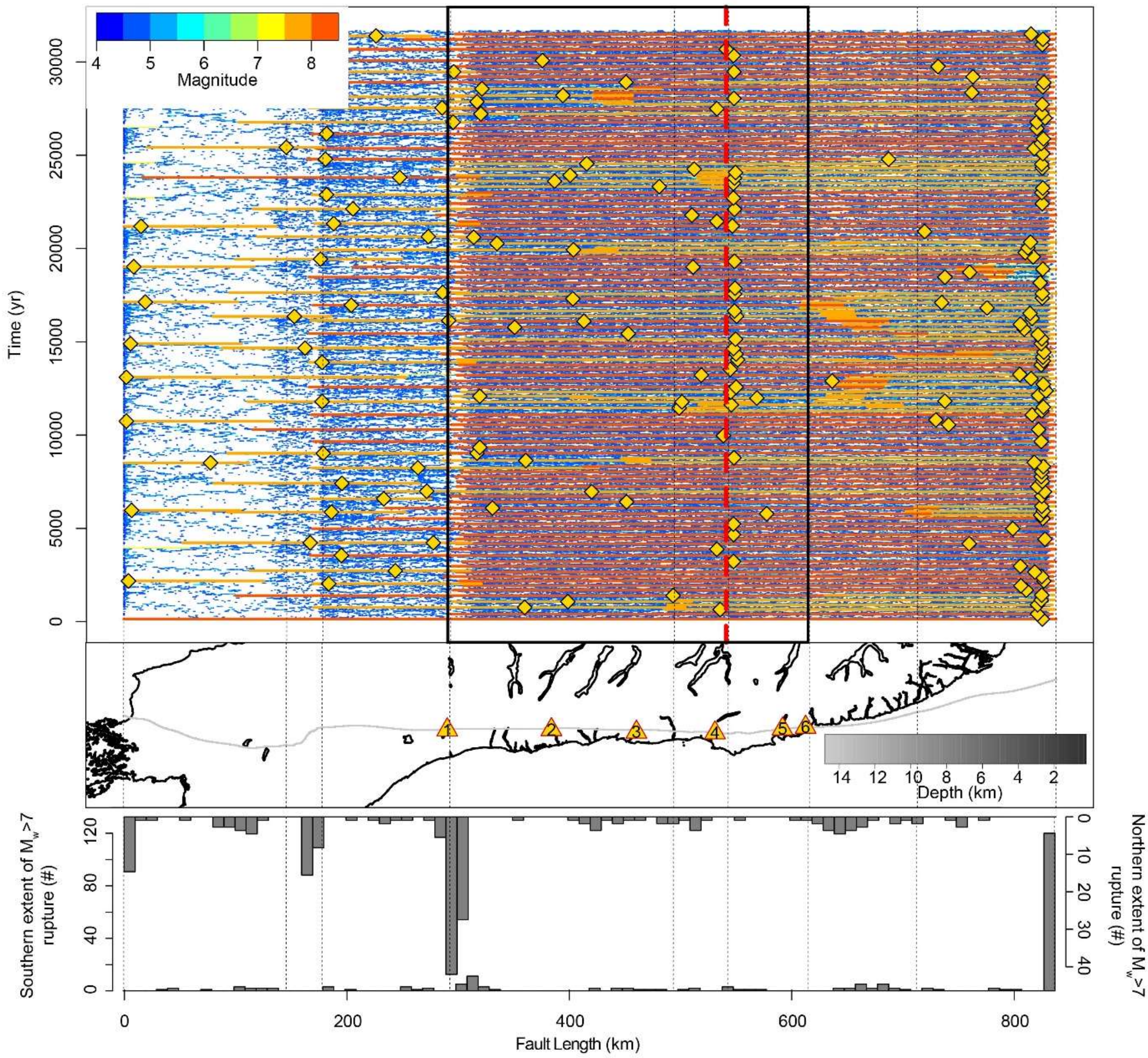

Supplementary Figure 11: Complete earthquake catalog (M_w>4) for the 33 kyr RSQSim Realistic Alpine Fault strike simulation (realistic kinematics and strike but constant seismogenic depth, vertical dip and homogeneous friction parameters). The black rectangle demarks the spatial extent of the paleoseismic data and the vertical red dashed line represents the location of the boundary between the Central and South Westland fault sections. Yellow diamonds indicate the epicenters of M_w>7 earthquakes. Numbered triangles in the middle panel show the location of the paleoseismic sites used in this study: 1) L. Kaniere, 2) L. Mapourika, 3) L. Paringa, 4) L. Ellery, 5) Hokuri Ck., and 6) John O'Groats R. The bottom panel shows the location and number of rupture terminations for earthquakes with M_w>7.

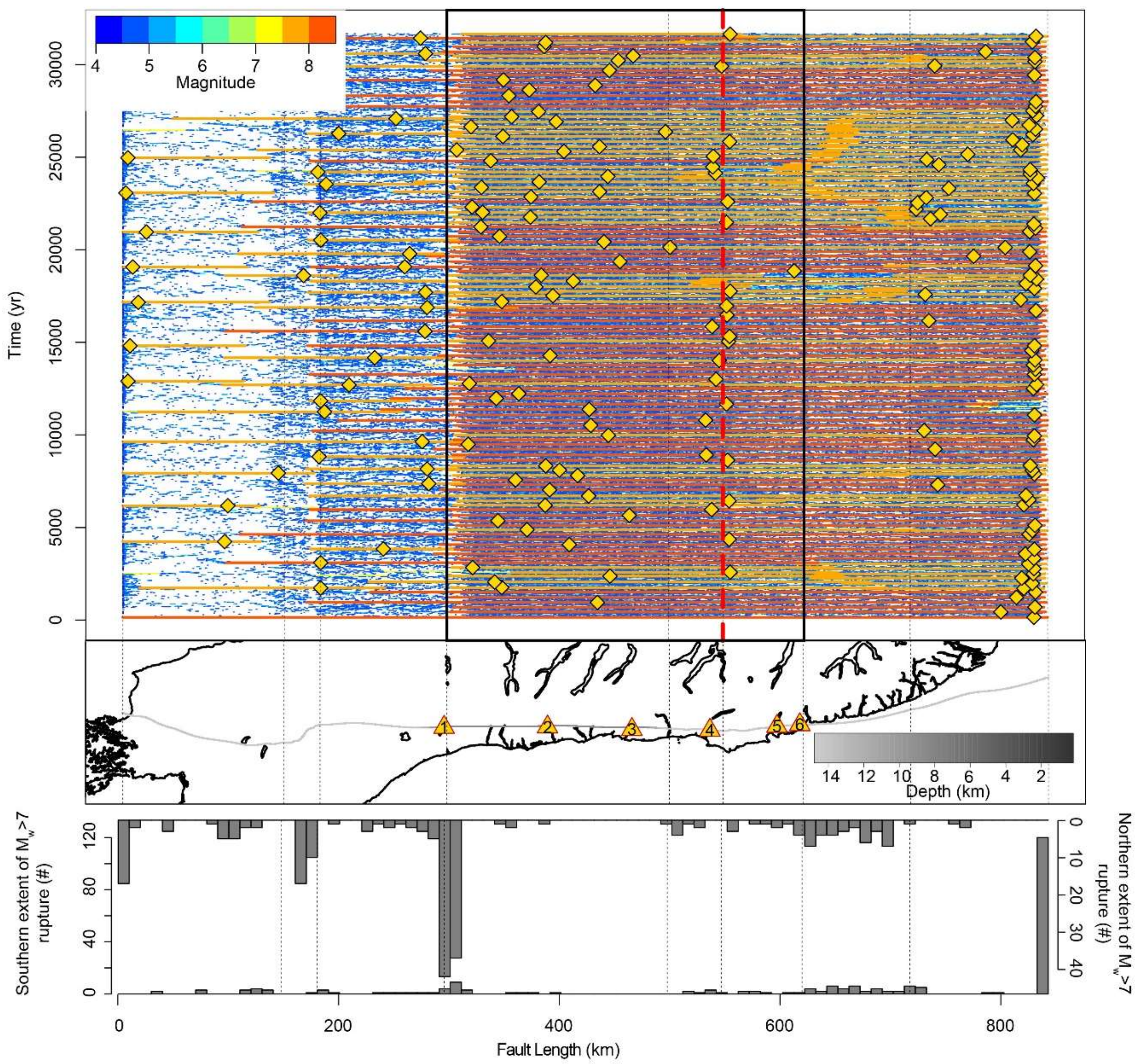

Supplementary Figure 12: Complete earthquake catalog (M_w>4) for the 33 kyr RSQSim Realistic Alpine Fault strike and seismogenic depth simulation (realistic kinematics, strike and seismogenic depth but vertical dip and homogeneous friction parameters). The black rectangle demarks the spatial extent of the paleoseismic data and the vertical red dashed line represents the location of the boundary between the Central and South Westland fault sections. Yellow diamonds indicate the epicenters of M_w>7 earthquakes. Numbered triangles in the middle panel show the location of the paleoseismic sites used in this study: 1) L. Kaniere, 2) L. Mapourika, 3) L. Paringa, 4) L. Ellery, 5) Hokuri Ck., and 6) John O'Groats R. The bottom panel shows the location and number of rupture terminations for earthquakes with M_w>7.

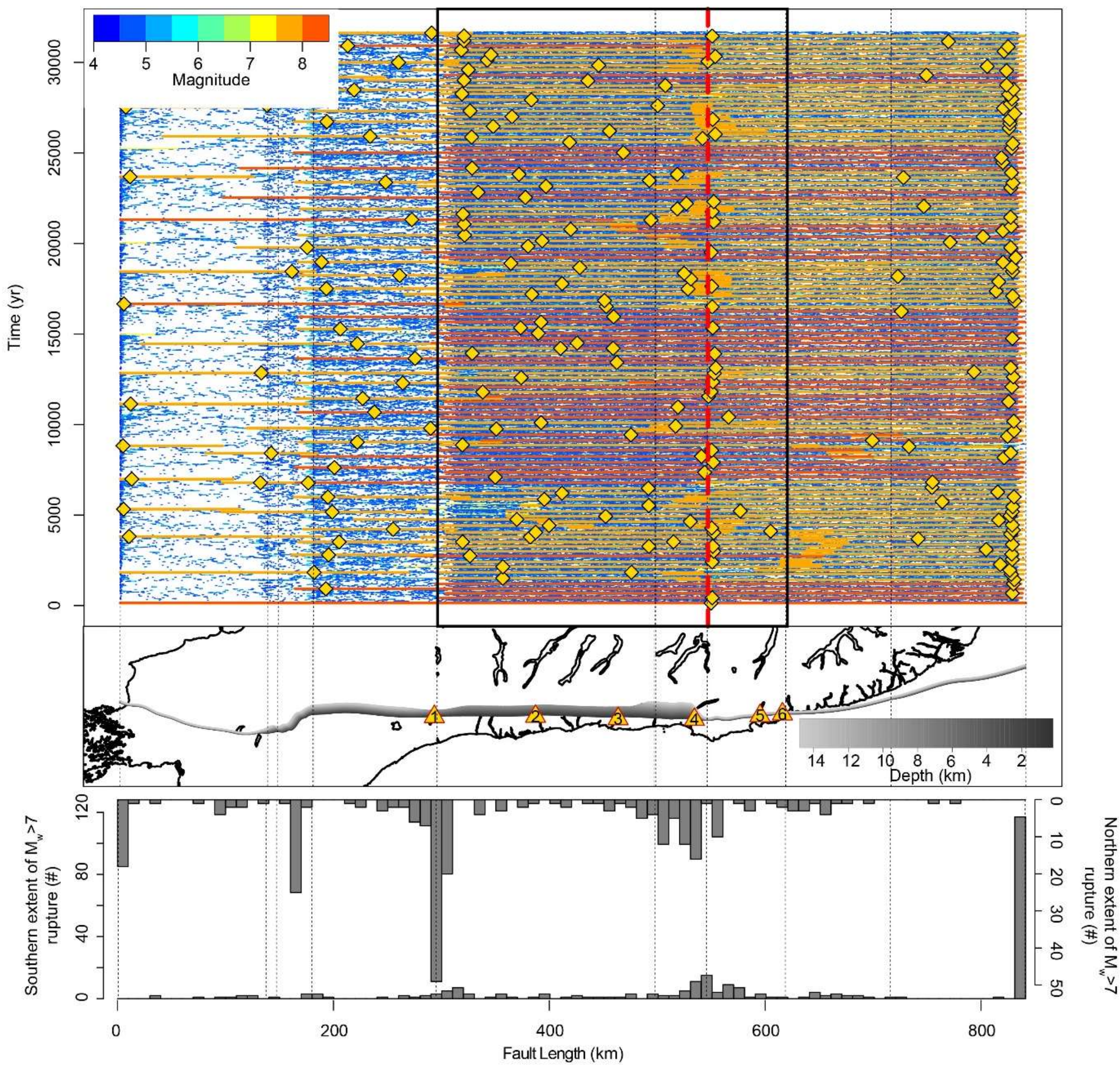

Supplementary Figure 13: Complete earthquake catalog (M_w>4) for the 33 kyr RSQSim Realistic Alpine Fault geometry simulation (realistic kinematics, geometry and homogeneous friction parameters). The black rectangle demarks the spatial extent of the paleoseismic data and the vertical red dashed line represents the location of the boundary between the Central and South Westland fault sections. Yellow diamonds indicate the epicenters of M_w>7 earthquakes. Numbered triangles in the middle panel show the location of the paleoseismic sites used in this study: 1) L. Kaniere, 2) L. Mapourika, 3) L. Paringa, 4) L. Ellery, 5) Hokuri Ck., and 6) John O'Groats R. The bottom panel shows the location and number of rupture terminations for earthquakes with M_w>7.

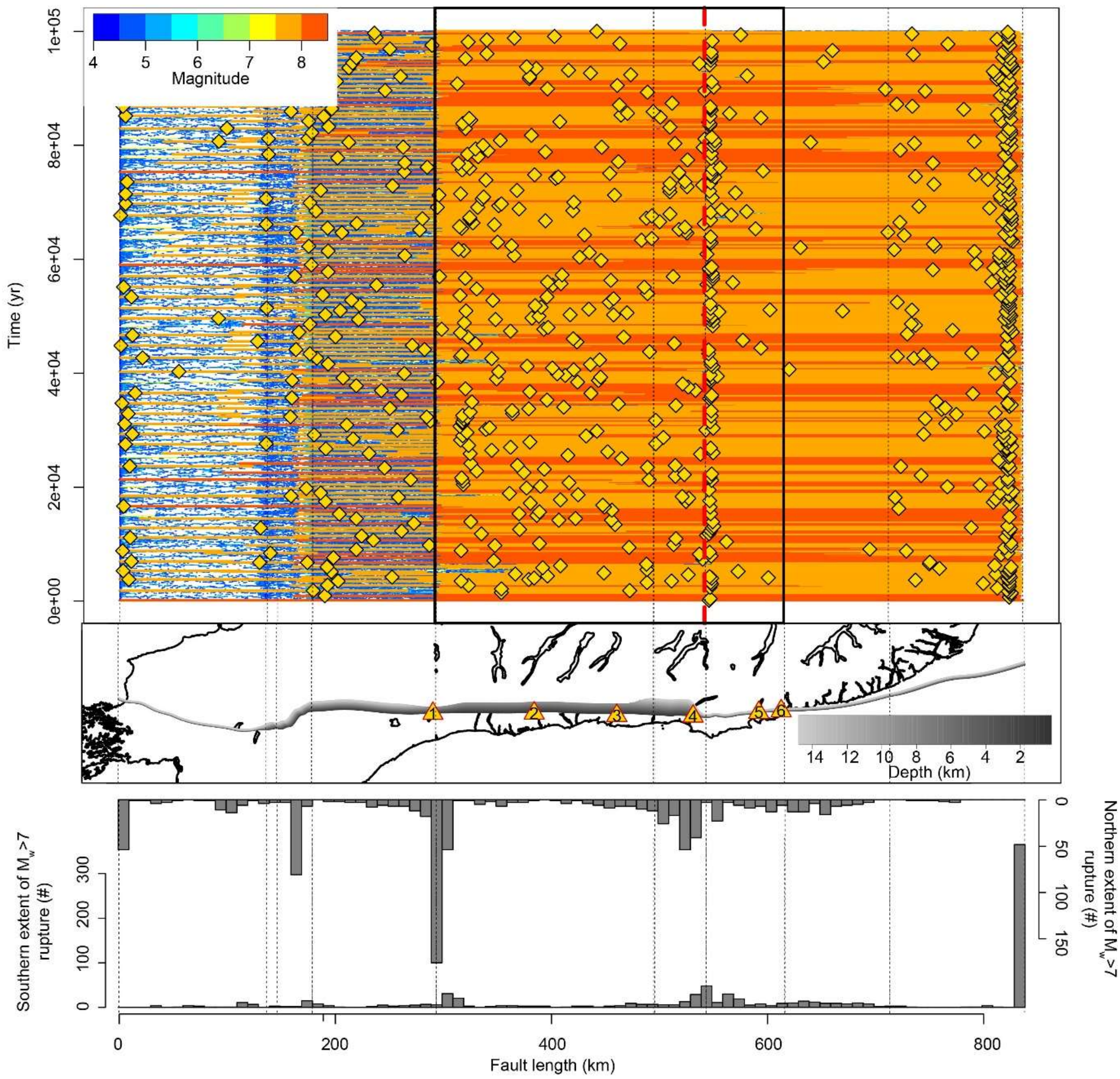

Supplementary Figure 14: Complete earthquake catalog (M_w>4) for the 100 kyr RSQSim Realistic Alpine Fault geometry simulation (realistic kinematics, geometry and homogeneous friction parameters). The black rectangle demarks the spatial extent of the paleoseismic data and the vertical red dashed line represents the location of the boundary between the Central and South Westland fault sections. Yellow diamonds indicate the epicenters of M_w>7 earthquakes. Numbered triangles in the middle panel show the location of the paleoseismic sites used in this study: 1) L. Kaniere, 2) L. Mapourika, 3) L. Paringa, 4) L. Ellery, 5) Hokuri Ck., and 6) John O'Groats R. The bottom panel shows the location and number of rupture terminations for earthquakes with M_w>7.

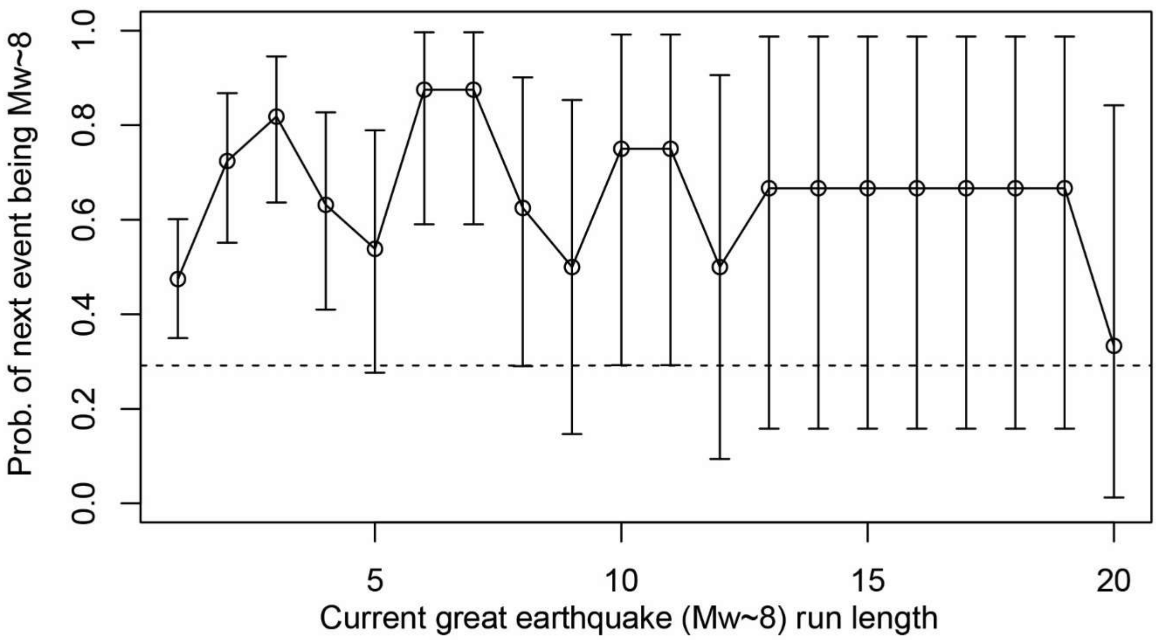

Supplementary Figure 15: Probability of an M_w~8 earthquake on the Central and South Westland sections given the number of earthquakes that have previously occurred in a mode of M_w~8 earthquakes. The x axis is the number of great earthquakes in a mode of multi-section ruptures. The dashed line is the probability for random occurrence of M_w~8 ruptures and the error bar represent a 95% confidence limit on the mean value. Values are derived from the 100 kyr Realistic Alpine Fault geometry simulation. The paleoseismic data suggest that the fault is three earthquakes into a mode of great multi-section earthquakes that ruptured through the Central-South Westland section boundary. Using the length of the current mode from the paleoseismic data and the 100 kyr simulation, we find that there is an 82 (+13/-18) % probability that the next rupture of the Central section will also involves the South Westland section in a M_w>8 earthquake and an 18 (+18/-13) % probability that it will be isolated to the Central section.

Supplementary Table 9: Conditional probabilities of rupture in the next 50 years from 2018 for the Central and South Westland sections derived using parametric and non-parametric methods (see Methods). All values in percent. 95% uncertainty bounds in parentheses.

Data source	Parametric (%)	Non-parametric (%)
Central Paleoseismology	68 (47, 92)	75 (29, 99)
South Westland Paleoseismology	40 (25,66)	43 (12, 78)

References:

1 Howarth, J. D., Fitzsimons, S. J., Norris, R. J., Langridge, R. & Vandergoes, M. J. A 2000 yr rupture history for the Alpine fault derived from Lake Ellery, South Island, New Zealand. *Geological Society of America Bulletin* **128**, 627-643, doi:10.1130/b31300.1 (2016).

2 Howarth, J. D., Fitzsimons, S. J., Norris, R. J. & Jacobsen, G. E. Lake sediments record high intensity shaking that provides insight into the location and rupture length of large earthquakes on the Alpine Fault, New Zealand. *Earth and Planetary Science Letters* **403**, 340-351, doi:10.1016/j.epsl.2014.07.008 (2014).

3 Howarth, J. D., Fitzsimons, S. J., Norris, R. J. & Jacobsen, G. E. Lake sediments record cycles of sediment flux driven by large earthquakes on the Alpine fault, New Zealand. *Geology* **40**, 1091-1094, doi:10.1130/g33486.1 (2012).

4 Waldmann, N. *et al.* Holocene mass-wasting events in Lago Fagnano, Tierra del Fuego (54°S): implications for paleoseismicity of the Magallanes-Fagnano transform fault. *Basin Research* **23**, 171-190, doi:10.1111/j.1365-2117.2010.00489.x (2011).

5 Schnellmann, M., Anselmetti, F. S., Giardini, D., McKenzie, J. A. & Ward, S. N. Prehistoric earthquake history revealed by lacustrine slump deposits. *Geology* **30**, 1131-1134 (2002).

6 Hovius, N. *et al.* Prolonged seismically induced erosion and the mass balance of a large earthquake. *Earth and Planetary Science Letters* **304**, 347-355, doi:10.1016/j.epsl.2011.02.005 (2011).

7 Avsar, U., Hubert-Ferrari, A., De Batist, M. & Fagel, N. A 3400 year lacustrine paleoseismic record from the North Anatolian Fault, Turkey: Implications for bimodal recurrence behavior. *Geophysical Research Letters* **41**, 377-384, doi:10.1002/2013gl058221 (2014).

8 Wang, J. *et al.* Controls on fluvial evacuation of sediment from earthquake-triggered landslides. *Geology* **43**, 115-118, doi:10.1130/G36157.1 (2015).

9 Van Daele, M. *et al.* A revised classification and terminology for stacked and amalgamated turbidites in environments dominated by (hemi)pelagic sedimentation. *Sedimentary Geology* **357**, 72-82, doi:10.1016/j.sedgeo.2017.06.007 (2017).

10 Talling, P. J., Masson, D. G., Sumner, E. J. & Malgesini, G. Subaqueous sediment density flows: Depositional processes and deposit types. *Sedimentology* **59**, 1937-2003, doi:10.1111/j.1365-3091.2012.01353.x (2012).

11 Debret, M. *et al.* Spectrocolorimetric interpretation of sedimentary dynamics: The new “Q7/4 diagram”. *Earth-Science Reviews* **109**, 1-19, doi:http://dx.doi.org/10.1016/j.earscirev.2011.07.002 (2011).

12 Disnar, J. R., Guillet, B., Keravis, D., Di-Giovanni, C. & Sebag, D. Soil organic matter (SOM) characterization by Rock-Eval pyrolysis: scope and limitations. *Organic Geochemistry* **34**, 327-343, doi:http://dx.doi.org/10.1016/S0146-6380(02)00239-5 (2003).

13 Ramsey, C. B. Radiocarbon calibration and analysis of stratigraphy: The OxCal program. *Radiocarbon* **37**, 425-430 (1995).

14 Langridge, R. M. *et al.* The New Zealand Active Faults Database. *New Zealand Journal of Geology and Geophysics* **59**, 86-96, doi:10.1080/00288306.2015.1112818 (2016).

15 Cox, S. C., Stirling, M. W., Herman, F., Gerstenberger, M. & Ristau, J. Potentially active faults in the rapidly eroding landscape adjacent to the Alpine Fault, central Southern Alps, New Zealand. *Tectonics* **31**, doi:10.1029/2011TC003038 (2012).

16 Wallace, L. M., Beavan, J., McCaffrey, R., Berryman, K. & Denys, P. Balancing the plate motion budget in the South Island, New Zealand using GPS, geological and seismological datas. *Geophysical Journal International* **168**, 332-352, doi:10.1111/j.1365-246X.2006.03183.x (2007).

17 Sutherland, R. *et al.* in *A Continental Plate Boundary: Tectonics at South Island, New Zealand* 235-251 (American Geophysical Union, 2007).

18 Hovius, N., Stark, C. P. & Allen, P. A. Sediment flux from a mountain belt derived by landslide mapping. *Geology* **25**, 231-234, doi:10.1130/0091-7613(1997)025<0231:sffamb>2.3.co;2 (1997).

19 Van Daele, M. *et al.* A comparison of the sedimentary records of the 1960 and 2010 great Chilean earthquakes in 17 lakes: Implications for quantitative lacustrine palaeoseismology. *Sedimentology* **62**, 1466-1496, doi:10.1111/sed.12193 (2015).

20 Stein, R. S., Barka, A. A. & Dieterich, J. H. Progressive failure on the North Anatolian fault since 1939 by earthquake stress triggering. *Geophysical Journal International* **128**, 594-604, doi:10.1111/j.1365-246X.1997.tb05321.x (1997).
21 Hogg, A. G. *et al. SHCal13 Southern Hemisphere Calibration, 0–50,000 Years cal BP*. (2013).
22 Ramsey, C. B. & Lee, S. Recent and planned developments of the program OxCal. *Radiocarbon* **55**, 720-730 (2013).
23 Berryman, K. R. *et al.* Major earthquakes occur regularly on an isolated plate boundary fault. *Science* **336**, 1690-1693, doi:10.1126/science.1218959 (2012).
24 Cochran, U. A. *et al.* A plate boundary earthquake record from a wetland adjacent to the Alpine fault in New Zealand refines hazard estimates. *Earth and Planetary Science Letters* **464**, 175-188, doi:10.1016/j.epsl.2017.02.026 (2017).
25 De Pascale, G. P., Quigley, M. C. & Davies, T. R. H. Lidar reveals uniform Alpine fault offsets and bimodal plate boundary rupture behavior, New Zealand. *Geology* **42**, 411-414, doi:10.1130/g35100.1 (2014).
26 De Pascale, G. P. & Langridge, R. M. New on-fault evidence for a great earthquake in AD 1717, central Alpine fault, New Zealand. *Geology* **40**, 791-794, doi:10.1130/g33363.1 (2012).
27 Wells, A., Yetton, M. D., Duncan, R. P. & Stewart, G. H. Prehistoric dates of the most recent Alpine fault earthquakes, New Zealand. *Geology* **27**, 995-998, doi:10.1130/0091-7613(1999)027<0995:PDOTMR>2.3.CO;2 (1999).
28 Bradley, B. A. *et al.* Ground motion simulations of great earthquakes on the Alpine Fault: effect of hypocentre location and comparison with empirical modelling. *New Zealand Journal of Geology and Geophysics* **60**, 188-198, doi:10.1080/00288306.2017.1297313 (2017).
29 Clark, K. J. *et al.* Deriving a long paleoseismic record from a shallow-water holocene basin next to the Alpine fault, New Zealand. *Bulletin of the Geological Society of America* **125**, 811-832, doi:10.1130/B30693.1 (2013).
30 Allam, A. A., Kroll, K. A., Milliner, C. W. D. & Richards-Dinger, K. B. Effects of Fault Roughness on Coseismic Slip and Earthquake Locations. *Journal of Geophysical Research: Solid Earth* **124**, 11336-11349, doi:10.1029/2018jb016216 (2019).
31 Barnes, P. M. Postglacial (after 20 ka) dextral slip rate of the offshore Alpine fault, New Zealand. *Geology* **37**, 3-6, doi:10.1130/g24764a.1 (2009).
32 Barth, N. C. *et al.* New c. 270 kyr strike-slip and uplift rates for the southern Alpine Fault and implications for the New Zealand plate boundary. *Journal of Structural Geology* **64**, 39-52, doi:10.1016/j.jsg.2013.08.009 (2014).
33 Norris, R. J. & Cooper, A. F. The Alpine Fault, New Zealand: surface geology and field relationships. *A Continental Plate Boundary: Tectonics at South Island, New Zealand*, 157-175 (2007).
34 Barth, N. C., Boulton, C., Carpenter, B. M., Batt, G. E. & Toy, V. G. Slip localization on the southern Alpine Fault, New Zealand. *Tectonics* **32**, 620-640, doi:10.1002/tect.20041 (2013).
35 Berryman, K. *et al.* Late Holocene Rupture History of the Alpine Fault in South Westland, New Zealand. *Bulletin of the Seismological Society of America* **102**, 620-638, doi:10.1785/0120110177 (2012).